Quantifying flow in variably wet microporous carbonates using object-based geological modelling and both lattice-Boltzmann and pore network fluid flow simulations

Quantifying flow in variably wet microporous carbonates using object-based geological modelling and both lattice-Boltzmann and pore network fluid flow simulations

Harland. S.R.[1], Wood. R.A.[1], Curtis. A.[1], van Dijke. M.I.J.[2], Stratford. K.[3], Jiang. Z.[2], Kallel. W.[2], Sorbie. K.[2]

[1]School of GeoSciences, University of Edinburgh, West Mains Road, Edinburgh, EH9 3JW

[2]Institute of Petroleum Engineering, Heriot-Watt University, Riccarton, EH14 4AS

[3]EPCC, University of Edinburgh, JCMB, Mayfield Road, Edinburgh, EH9 3JZ

Acknowledgements

The authors are grateful to the sponsors of this Industry Technology Facilitator (ITF) project BG Group, Chevron, Dong Energy and Wintershall for funding and for permission to publish this work. We thank the Edinburgh Parallel Computing Centre (EPCC) for allowing access to the BGQ machine and computational time. Kevin Stratford acknowledges support from UK EPSRC grant EP/J007404.

ABSTRACT

Chalky microporosity can constitute up to 100% of the total porosity within carbonate reservoirs, but its contribution to both single- and multi-phase flow is poorly quantified. We present a flexible, object-based algorithm to construct 3D computational rock representations that reproduce micritic fabrics of chalky microporous carbonates based on calcite crystal fabrics observed in 2D SEM images. By methodologically altering model parameters we begin to explore the state-space of microporous carbonates to quantify single- and multi-phase flow using both lattice-Boltzmann and network flow models.

Micropore size has little to no effect on single-phase permeability, while differences in multi-phase flow properties are observed for microporous fabrics with pores no smaller than 0.50μm^3 suggesting a change in the pore-scale controls on flow. Single-phase permeability increases by an order of magnitude within fabrics of varying total microporosity (18% to 35%), but minimal effect on multi-phase flow is observed. Similarly, multi-phase flow properties are unaltered by micrite rounding due to burial dissolution, suggesting no alteration in pore-network topology. Micrite rounding, however, notably increases porosity and single-phase permeability in comparison to original rhombic micrite fabrics. The presence of moldic mesopores impacts flow but only when there is a direct connection between them. Otherwise, single-phase permeability is controlled by micropores. Importantly, recovery is dependent on wetting scenario and pore-network homogeneity. Under water-wet imbibition, an increase in pore homogeneity (more micropores) yields a lower residual oil saturation. Together, these results quantify the importance of microporosity in contributing to, or controlling, overall flow and sweep characteristics in carbonate reservoirs.

1. Introduction

Understanding the pore system and petrophysical properties of subsurface reservoir rocks is vital for accurate prediction of fluid flow behaviour and therefore hydrocarbon recovery. Predicting such properties for carbonate rocks can be a particularly complex task as their pore systems are inherently multi-scale, often spanning four relevant orders of magnitude of pore size variation (Choquette and Pray, 1970). Perhaps the least understood type of porosity within carbonates is microporosity. There are many definitions of the class of microporosity, including pores <10μm in diameter and hence below the resolution of an optical microscope (Cantrell and Hagerty, 1999), or pores less than 62.5μm in diameter (Choquette and Pray, 1970), or pores less than 1μm in diameter in at least one direction (Pittman, 1971).

Microporosity has many origins, but the most pervasive form of microporosity is known as 'chalky' microporosity (Pittman, 1979; Moshier, 1989a; Budd, 1989). Chalky microporosity is formed between the crystal faces of rhombic micrite (micro-crystalline calcite, Figure 1a; see Folk, 1962) which is thought to form through the transformation of acicular high-magnesium calcite and aragonite lime mud crystals into micro-rhombic low-magnesium calcite (Lucia and Loucks, 2013). This occurs via dissolution and recrystallization, although the exact details of the process are still debated (Dravis, 1989; Cantrell and Hagerty, 1999; Heasley et al., 2000; Lambert et al. 2006, Lucia and Loucks, 2013). These pores have a distinct 'plate-like' morphology (Cantrell & Hagerty, 1999) and one spatial dimension maybe up to an order of magnitude smaller than the other two dimensions (Figure 1b, inset) where in the smallest dimension the pores are 0.1μm while in the other two dimension they are around 1μm. Nevertheless, such pores may constitute a significant percentage of the total porosity and of the potential storage capacity (up to 100% in mud dominated facies) of some of the largest known carbonate reservoirs, for example the Middle Eastern Upper Jurassic Arab Formation (Cantrell & Hagerty, 1999; Lambert et al., 2006) and the Lower Cretaceous Thamama group (Moshier, 1989b; Budd, 1989; Smith et al., 2003; Lambert et al., 2006; Cox et al., 2010; Deville de Periere, 2011).

Relatively few studies have attempted to quantify the contribution of microporosity to both single- and multi-phase flow. Consequently the resultant effects on petrophysical properties are neither routinely acknowledged or accounted for when assessing reservoir quality. For example, it is commonly assumed that hydrocarbons are unlikely to be emplaced into micropores during primary drainage (due to the small throat diameters, typically <1μm, and resultant high capillary), and that microporosity therefore contributes very little to fluid flow through the reservoir unit, containing only bound, irreducible waters (Pittman, 1971; Kirkham et al., 1996; Cantrell and Hagerty, 1999). Recently, however, the potential importance of micropores has been highlighted by several authors who have

77 shown that it is possible for hydrocarbons to be contained within micropores, especially
78 towards the top of the oil column (Cantrell & Hagerty, 1999; Lambert et al., 2006). Studies
79 have also shown that micropores can influence fluid flow by either decreasing residual oil
80 saturation (Wu et al., 2008; Hollis et al., 2011; Fullmer et al., 2014) or by providing the
81 permeable pathway between otherwise disconnected, larger scale pores (Roth et al.,
82 2011). While micropore-dominated carbonates have low permeabilities (less than 10mD),
83 the pervasive distribution of microporosity has been shown to result in a higher sweep
84 efficiency within intervals with a high percentage of micropores (Wu et al., 2008; Hollis,
85 2011; Fullmer et al., 2014). Additionally, within some multiscale pore networks, micropores
86 provide the connectivity and fluid pathway between larger scales of porosity (Figure 1b).
87 For example, Roth et al. (2011) demonstrated that connectivity through a multi-scale
88 carbonate pore network was only achieved when pores <12μm in diameter were present in
89 the model; in these models, the microporosity actually controlled the percolation threshold.
90 Hence, it is important that the contribution of chalky microporosity to flow is understood
91 and quantified in order for accurate reservoir property predictions to be made.

92 Chalky microporous carbonates have many different fabric properties which can vary
93 throughout a reservoir, and micropore morphology (size and shape) is controlled by the
94 different styles of packing and size distribution of the micrite crystals (Lambert, 2006;
95 Volery, 2010; Deville de Periere, 2011; Fullmer et al., 2014). Microporosity can be found,
96 for example, within micritised grains, or as pervasive horizons of micritic matrix (with or
97 without larger mesopores), or between grains where the inter-granular pore space has
98 been micritised (Cantrell and Hagerty, 1999). An additional feature of some microporous
99 carbonates, particularly those in the Middle East, is micritic dissolution (Budd, 1989;
100 Moshier, 1989b; Wagner, 1990) which is typically found towards the top of the oil column
101 (Lambert et al., 2006). Acidic fluids flowing through the micropore network prior to
102 hydrocarbon emplacement, dissolve the edges and vertices of the rhombic micrite crystals

103 to leave rounded crystals (Figure 1c) with a reduced crystal size (Lambert, 2006).
104 Microporous horizons with rounded crystals due to micritic dissolution have been shown to
105 have better reservoir qualities (high porosity and single-phase permeability) than their
106 rhombic counterparts, and have between 8% and 13% more porosity (Lambert, 2006).
107 However, the effect of micritic dissolution on multi-phase flow properties is unknown.

108 These observations suggest that further research is required on variations in microporous
109 fabric properties and the effects that they have on flow, both individually and in
110 combination. As such, building a flexible computational algorithm to produce digital rock
111 models that incorporate the textural variations of microporous carbonates provides a
112 useful methodology.

113 To understand the flow properties of chalky microporosity, 3D images from computer
114 tomography (XMT) scanners (Van Geet et al., 2000) would be ideal. Chalky microporosity,
115 however, is below the resolution of standard micro-computer tomography (μ-CT) scanners,
116 and although nano-CT scanners (resolution <100nm^3/voxel) are capable of imaging
117 microporosity, the sample volumes (<15μm^3) are too small to acquire a statistically
118 significant dataset. Direct 3D images also provide very little flexibility to study the effect on
119 flow of variations in microporosity as the properties of the rock fabric in the image cannot
120 be adjusted with ease, if at all. As such, rock reconstruction methods that focus on
121 reproducing geological fabrics to infer the pore-space, provide a more viable and flexible
122 methodology. Indeed, the pore network of a rock is created by its fabric, so by accurately
123 reconstructing the solid phase(s), the pore network and therefore the petrophysical flow
124 characteristics (e.g., porosity, absolute permeability, relative permeability and capillary
125 pressure curves) of the medium can be determined.

126 Many different methodologies have been developed to produce 3D models of porous
127 media. For example, there are object-based modelling methods including process-based

128 reconstructions (Bakke and Øren, 1997; Øren and Bakke, 2003) and continuum based
129 reconstructions (Biswal et al. 2007; 2009a,b) and there are statistical or stochastic
130 reconstructions from 2D images (Okabe and Blunt, 2004; Al-Kharusi and Blunt, 2008; Wu
131 et al., 2004, 2006; 2008).

132 While all proposed methods provide advantages for certain applications, they have
133 limitations for modelling microporosity. For example, reconstructions based on the spatial
134 statistics of 2D images can be used to create 3D models using multipoint-statistic
135 techniques (Okabe and Blunt, 2004; Al-Kharusi and Blunt, 2008) or stochastic approaches
136 involving Markov meshes (Wu et al., 2004, 2006; 2008). These statistical approaches,
137 however, tend to smooth the true variations in the image structure, and as such fail to
138 capture the heterogeneous nature of multiscale pore systems such as those within
139 carbonates. Object-based models provide perhaps the most flexible basis for modelling
140 rock fabrics as the fabrics can be altered and adjusted to recreate all geological variability
141 based on observations. However, the complex processes of carbonate diagenesis mean
142 that process-based modelling methodologies, which work very well for reconstructing
143 sandstones (Bakke and Øren, 1997; Øren and Bakke, 2003), are problematic to implement
144 for carbonates. For an application of the method to chalky microporosity in particular, the
145 diagenetic process of formation of micrite is not only poorly understood, but may also vary
146 from reservoir to reservoir (Budd, 1989; Moshier, 1989a; Moshier, 1989b; Cantrell and
147 Hagerty, 1999; Lambert et al., 2006; Richard et al., 2007; Volery et al., 2009; Lucia and
148 Loucks, 2013). While continuum based modelling methodologies (e.g. Biswal et al. 2007;
149 2009a,b) provide a unique approach which combines low resolution micro-CT scans with
150 2D geological/crystal information in a continuum object-based technique to reproduce
151 carbonate fabrics at multiple resolutions, such an approach did not produce models with a
152 resolution high enough to examine microporosity, limiting quantification of the effect of
153 microporosity on the petrophysical flow properties of the rocks in question (Roth et al.,

2011).

In this study, we present an object-based digital rock building methodology that aims to accurately reconstruct the fabric of chalky microporous carbonates in order to accurately capture relevant statistical properties of the pore space. Both quantitative and qualitative underlying data are used to populate the models based on data from 2D SEM image analysis. The algorithm is flexible such that it can model the textural variations of microporous carbonates and include multiple scales of porosity. This new methodology is thus able to reconstruct reservoir rocks at a resolution capable of capturing microporosity, enabling interrogation of both single-phase and multi-phase flow in chalky microporous carbonates.

In what follows, we use the algorithm in combination with a lattice-Boltzmann simulator, a network extraction algorithm and a multi-phase phase flow simulator to study the single- and multi-phase flow properties of synthetically generated typical Middle Eastern chalky microporous carbonates. In particular, we consider the effect of micropore size, total micropore content and the effect of micritic dissolution within models of purely micritic matrix. Finally, we examine how moldic mesoporosity within a microporous network affects the flow properties of synthetically generated multiscale pore networks.

2. METHODOLOGY

2.1. Textural Properties of Micrite and Micropores

The 3D model needs to be calibrated with geostatistical data. Since it is not possible to image chalky microporosity directly using 3D scanning methods, following other studies (Biswal et al., 2007, 2009a, 2009b; Deville de Periere et al., 2011) we use scanning electron microscope (SEM) images to capture the basic textural properties of microporous carbonates. Image analysis is performed using IMAGEJ (Schneider et al., 2012).

Different types of SEM images are used to extract both quantitative and qualitative data to

calibrate the models. Secondary electron images (Figure 1) provide a shallow, pseudo 3D image of rough cut chips which allows the crystal form and the nature of the contact between crystals to be examined. For example, the micrite in the chalky microporosity sample in Figure 1a consists of approximately equidimensional euhedral rhomboids, often with multiple facets, and there is no obvious alignment of crystal orientation.

Images of epoxy resin pore casts (Figure 1b) are used provide insight into the form, size and distribution of different pore types (macropore and micropore) within a sample. They also provide crucial information about the nature of 3D connectivity between pores. For example, the highly connected sponge-like network of platy microporosity, and the connectivity between this network and a mesopore, can be seen in Figure 1b.

Finally, backscatter images of highly polished, flat sample surfaces (Figure 2a,b) provide a good contrast between pore and solid. They enable easy binarisation to determine 2D slice porosities and also allow measurements of crystal diameter to be made within the image plane. SEM images are taken at a very high resolution (here up to 0.10μm/pixel) and as such, before any crystal diameter data are extracted through image analysis, the resolution of the SEM image needs to be reduced (by averaging across neighbouring pixels) to match that of the models which will be built. This removes features that would be unresolvable at the model resolution.

After binarisation and resolution reduction, a watershed algorithm can be applied to detect individual crystals and Feret diameter measurements (with amalgamated crystals removed) can be made to provide a quantitative crystal size distribution (Figure 2c) from which the model can be populated. Where it is not possible to detect crystal edges through an automated process, manual measurements of the longest diagonal length of the crystal can be made instead. The resulting data are 2D crystal diameters. By collecting a statistically significant number of diameters (here, over 400 measurements) these are

assumed to be reflective to the 3D crystal diameters.

2.2 Object-Based Reconstruction Methodology

The crystal size distribution (Figure 2c) is used to build a library of 3D micrite crystals at the desired resolution, including forms rotated around the x, y and z axes at discrete intervals throughout the desired range of rotations. Micrite crystals have multiple facets and so a very high resolution digital model would be required to capture the crystal facets correctly. As such the rhombs are simplified to cubes; this maintains the approximately equidimensional and euhedral nature of micrite, but reduces the voxel resolution required to represent the crystal form. The algorithm is flexible such that if multiple crystal types, shapes and sizes were required, these could simply be included in the library.

When distributing the crystals, matrix connectivity is guaranteed by allowing (or forcing) an overlap of neighbouring crystals. Crystals in the library have a layered structure where voxels on the edges of the crystal are identified; these are allowed to overlap with other crystal edge voxels, while crystal centres must remain non-overlapping (Figure 3a, b). This technique has similarities to the ‘cherry-pit’ or penetrable-concentric-shell (PCS) model (Torquato 1984, 1985, 1986). As such, the smallest crystal size for any model resolution is 3^3 voxels to ensure both a distinct crystal centre and edge voxels (Figure 3c, d). The degree of overlap can be varied so as to suitably represent different micritic textures observed in samples. This allows different styles of micrite packing to be represented, but a minimum edge layer thickness of one voxel is required at any resolution, to maintain matrix connectivity.

The rock reconstruction is initialised within a 3D space, discretised into a grid of regular cubic voxels of a predefined physical size (the resolution). In an iterative process, voxels are defined as solid by randomly fitting micrite crystals from the library into the grid. This continues until a desired total percentage of solid, and therefore the desired total porosity

(ϕ_D) is achieved. Crystals are fitted from largest to smallest, with the number of iterations (N_i^C) of each crystal size (indexed by i) calculated based on the known crystal frequency distribution (f_i^C, as shown for example in Figure 2c), the volume of each crystal size (V_i^C), the total volume of the grid being filled (V), and the total porosity (ϕ) required in the final model which is related to ϕ_D as described below. As such the number of iterations of each crystal size required to achieve the target porosity is predetermined based on the ratio (R) between the volume of solid produced by the crystal size distribution and the volume of the model to be created as shown in Equations (1) and (2):

$$R = \frac{V}{(1-\phi)\times\sum_{i=1}^{n} V_i^C \times f_i^C} \quad (1)$$

$$N_i^C = R \times f_i^C \quad (2)$$

The overlapping edge voxels of the crystals result in an underestimate of the number of crystals required to fill the volume as overlapping edges are not accounted for in Equations (1) and (2), hence the resulting final porosity would always be higher than the required porosity. To account for this, the target porosity (ϕ in Equations (1) and (2)) is set at a value that is predictably lower than the desired porosity (ϕ_D). This prediction is based upon a sensitivity test to determine the average loss in solid voxels due to overlap at a desired porosity. An example is shown in Figure 4.

At each iteration, a random (possibly rotated) crystal of the correct dimensions is selected from the crystal library, and randomly selected potential grid locations are successively tested until a location that satisfies the edge and centre placement conditions is found. Upon completion, the algorithm results in a binary model (Figure 3b) of the foreordained porosity (φ_D) that is 100% microporosity and a solid proportion that is 100% micrite. Information specific to each crystal placed into the model such as crystal centre coordinates, crystal diameter and rotational information, is stored in an array as objects

are placed into the volume. This information may be used to manipulate the model fabrics to perform rounding of the micrite crystals to emulate micritic dissolution, or to include larger scale features such as mesoscale porosity (pores >10μm in diameter) and cements. The properties of mesopores and cements can be determined from the SEM images in a similar manner to the properties of micrite.

Micrite rounding is performed homogeneously across the model volume. The cubic form of the micrite crystals is altered to a spherical form by tracing the inscribed radius of the crystals based on their diameter. Because of the alteration to the fabric it is again important to ensure matrix connectivity of the rounded crystals. This is achieved by testing that each crystal touches at least one other. If this is not satisfied, slight shifts of the unconnected crystals are made to abut them against another crystal. In the highest porosity models generated for this study, this shift process affected less 0.4% of the crystals, but must nevertheless be performed to reflect the rock texture and avoid floating crystals in the matrix.

The purely microporous models can subsequently be merged, under certain conditions, with larger scale pores to generate multiscale networks. The mesopore networks can be derived from subsections of micro-CT images or can be synthetically generated to represent, for example, moldic mesopores. Moldic mesopores occur through the preferential dissolution of forams during burial and an example of such is a mould is shown in Figure 1b. The modelled moldic mesopores here are simplified to spherical bodies, although more complex shapes can be used. The size and location of the moulds within the modelled volume can be determined randomly or predefined.

Although this process of merging the two pore systems does not reflect the processes of formation of the mesopores and the micritic matrix, the fabrics generated do reflect those observed from SEM analysis such as the connectivity between mesopores and

277 microporosity (Figure 1b) and the rugosity around mesopore edges due to micrite crystals
278 (Figure 2b). The micrite crystals that exist around the edges of the mesopores can also be
279 used as nucleation sites for pore-occluding cements such as those seen in Figure 2b, but
280 we do not study that aspect of the pore system in this paper.

281 ### 2.3 Sensitivity Analysis of Fluid Flow Properties to Rock Fabric Properties

282 Here in we explore the variability of chalky microporous carbonate rocks to investigate the
283 flow properties of the different fabrics. First, we investigate the sensitivity of flow properties
284 to micropore size, controlled by varying the resolution at which each model is generated.
285 The size of micropores is likely to vary from reservoir to reservoir and also within any
286 individual reservoir. Models were generated at five different resolutions: 0.50μm^3/voxel,
287 0.40μm^3/voxel, 0.30μm^3/voxel, 0.20μm^3/voxel and 0.10μm^3/voxel, with three realisations
288 generated at each resolution. Each resolution model had a porosity of approximately 26%
289 and a volume of 400^3voxels and therefore the physical volume size varied between
290 models (Table 1). Both single- and multi-phase flow were simulated on the full 400^3voxel
291 volume models; however in order to be able to compare the properties of the different
292 fabrics properly, eight subvolumes of the four lowest resolution models were also isolated.
293 These subvolumes each had the same physical volume as the highest resolution model
294 (0.10μm^3/voxel) which had a volume of $40^3 \mu m^3$. The voxel sizes of these subvolume
295 models are shown in Table 1.

296 Secondly, we consider the effect on fluid flow of total porosity within a purely micritic (and
297 therefore purely microporous) fabric and also investigate the effect of micritic dissolution
298 on flow for varying total porosity. Within a microporous reservoir, the total microporosity
299 within micritic matrix varies (Fullmer et al., 2014) and models of varying total matrix
300 porosity were generated to interrogate the single-phase and multi-phase flow properties of
301 100% microporous fabrics. Total porosity was varied from 18% to 35% and three

realisations of each model were created. These porosities are within the range of reported values for purely microporous carbonates (Volery et al., 2010; Deville de Periere et al., 2011; Fullmer et al., 2014) and of porosities from SEM image analysis performed for this study. These models were created at a resolution of 0.40μm^3/voxel and were 400 voxels (or 160μm) in length. Here we also examine the effect of micritic dissolution on flow properties by performing micrite rounding on one model at each given porosity.

Finally, we investigate the effect of the presence of synthetic spherical moldic mesopores within a micritic matrix of varying total (micro- and meso-) porosity. Although fully microporous horizons do exist within reservoirs, it is additionally important to understand the range of multi-scale fabrics in which micropores do (and do not) contribute to flow. A mesopore was placed in each octant of a 400voxel^3 model generated at 0.40μm^3/voxel resolution. Amongst other properties, the size of forams varies and as such, the radii of the mesopores in the grid were varied between 10μm and 45μm, generating five different mesopore models. These mesopore models were combined with purely micritic matrices, with microporosities of 18%, 25% and 35%.

All models generated during this study were populated with crystals from the crystal size distribution extracted from SEM image analysis of samples (Figure 2c), discretised to the correct resolution in each of the above cases in order to create appropriate corresponding crystal libraries.

2.4 Simulation of flow

Two separate methodologies are employed to simulate single- and multi-phase flow in this paper. We describe each in turn.

2.4.1. Single-phase Flow Simulation

Single-phase flow simulation for the computation of absolute permeability is performed directly on the discretised model using a multiple relaxation time (MRT: Chun and Ladd,

2007) lattice-Boltzmann model (Ludwig: Desplat et al., 2001) which represents the boundaries of solid objects using a simple bounce-back scheme. Simulations are performed in lattice units (lu), and converted to SI units (mD) based on the true voxel size (Δx). A permeability is obtained by computing the steady-state volume flux in a periodic system (obtained by reflecting the volume along the flow direction and using periodic boundaries) generated by a constant body force with a viscosity (η) of 1/6 in all cases. The simulations were parallelised and used 2048 cores on the Blue Gene/Q supercomputer based at the Edinburgh Parallel Computing Centre.

The steady state volume flux (Q) is related to the macro-scale permeability (k) by the Darcy equation (Equation (3) below, Darcy, 1856) where the differential pressure ($P_b - P_a$) is related to the applied body force and the length of the system in the flow direction (L) of cross-sectional area (A) by

$$Q = -\frac{kA}{\eta}\frac{(P_b - P_a)}{L} \quad (3)$$

As is usual with this type of calculation, we ensure that the final pore-scale Reynolds number is below unity to simulate incompressible Newtonian, laminar flow. For the narrowest pores in the system, we would expect the flow to be poorly resolved which would lead to some systematic, and likely, underestimates in the permeability. Tests in capillaries with regular geometries (circular, triangular, square cross-section) suggest errors in computed permeability to be up to ≈25% for widths less than ~4Δx (Sengupta et al. 2012).

2.4.2. Multi-phase Flow Simulation

We perform multi-phase flow simulations on pore networks extracted from the generated models using the Pore Architecture Tool (PAT) algorithm developed by Jiang et al. (2007). This method is based on extracting the local medial axis through the pore space (using a thinning algorithm) and separating the network into pore bodies and throats (nodes and

351 bonds), preserving the connectivity and topological characteristics of the pore space.
352 Junctions in the network are defined as pore bodies (nodes) and the connecting pathways
353 between nodes are then throats (bonds). Quantitative geometrical characteristics of the
354 network elements such as pore radius, perimeter and area, shape factor and coordination
355 number (the number of bonds connecting to each node in the network), are all determined.
356 These geometrical properties control the development and stability of wetting layers within
357 the network elements (Blunt, 1998; Valvatne and Blunt, 2004). The topology (or
358 connectivity) of the network plays an important role in controlling the multi-phase flow of a
359 network and this can be described for the extracted pore network by calculating the
360 specific Euler number (χ, Vogel and Roth, 2001) which is simply the number of nodes (N)
361 minus the number of bonds (B) divided by the volume of the model (V):

$$\chi = \frac{N-B}{V} \qquad (4)$$

362 The Euler number can also be used to derive the pore size dependent connectivity
363 function by removing pores from the network in order of increasing size and recalculating
364 the Euler number at each step (Vogel and Roth, 2001). Removing larger and larger pores
365 will eventually result in a positive Euler number (fewer bonds than nodes) which indicates
366 the point at which the network becomes unconnected and as such an Euler number of
367 zero is a proxy for the percolation radius of the network.

368 Multi-phase flow was simulated on the extracted networks using the quasi-static (capillary
369 dominated flow) Poreflow software (Valvatne and Blunt, 2004) where two-phase flow is
370 simulated according to invasion-percolation principles during drainage (invasion of oil) and
371 imbibition (invasion of water). A pressure gradient is applied to each phase across the pore
372 network (between the inlet and outlet face) and the relative permeabilities of each phase
373 are determined by calculating the pressure distribution in response to the change in
374 pressure gradient across each phase, using mass conservation, at each node (Øren et al.,

375 1998).

376 In order to simulate multi-phase flow, the pore-scale wetting properties of the model must
377 be predefined. However, the wetting properties of carbonates and microporosity are poorly
378 understood. Strong variations of wettability in different reservoirs are observed more
379 frequently in carbonate reservoirs than in siliciclastic reservoirs (Bobek et al., 1958) and
380 studies into the wettability of globally distributed carbonates (e.g. Treiber and Owens,
381 1972; Kashfi, 1974; Morrow, 1976; Chillingar and Yen, 1983; Cuiec, 1984) have indeed
382 produced varying results. But at the core plug scale, most carbonates have been found to
383 have an intermediate wetting state (Skauge et al. 2006), i.e. they have a weak affinity
384 towards oil. Estimating wettability at the core plug scale is a complex task in itself and few
385 studies have been able to examine the wettability distribution at the pore scale. Here, two
386 different imbibition (water flood) wettability scenarios at the pore scale were simulated to
387 characterise concomitant variations in the multi-phase flow properties. For both scenarios,
388 the pore network is initially assumed to be strongly water-wet and oil flooding (water
389 drainage) continues until a residual water saturation of 0.02 has been achieved. For the
390 first imbibition scenario, the rock remains water wet after drainage and no aging occurs.
391 The second imbibition wettability scenario was performed under a simple fractionally wet
392 scenario where 50% of the pores become oil-wet after drainage (due to aging). This type
393 of wetting is neither pore shape nor pore size dependent, and the oil wet-network elements
394 are randomly distributed throughout the network. Imbibition continues until a minimum
395 residual oil is achieved.

396 ## 3. Results

397 ### 3.1 Effect of Micropore Size

398 #### 3.1.1. Model Fabric Properties

399 As can be seen from Figure 5, the morphology of the micritic fabric in the model matches
400 well with that which is observed in the SEM image.

401 Figure 6 shows 2D slices through a 3D realisation at each resolution, scaled relative to
402 their physical sizes. Visually the models can be seen to be producing very similar micritic
403 fabrics, the simple difference being that the pores and crystal are represented by an ever
404 increasing number of voxels as resolution is increased from 0.50μm^3/voxel up to
405 0.10μm^3/voxel (a to e respectively in Figure 6), and the size of the smallest resolvable
406 feature decreases with each increase in resolution.

407 **3.1.2. Pore Network Properties**

408 The pore radii distributions shown in Figure 7a indicate the change in pore geometry with
409 model resolution. The box in Figure 7a shows the smallest pores in the generated models
410 and these pores are equal to the resolution of the model (half a voxel in radius). As the
411 resolution is decreased progressively from 0.10 to 0.50 μm^3/voxel, the smallest pores are
412 lost from the volumes and (at the other end of the scale) larger pores are incorporated.
413 This is reflected in the increase in the average pore radius with a decrease in resolution
414 (Table 2) and an increase in the upper limit of the pores captured by the models (Figure
415 7a).

416 The percolation radius (where the Euler number is 0) can be seen to be dependent on
417 model resolution. The models generated at 0.10-0.40μm^3/voxel have a percolation radius
418 of ~0.3μm while the model at 0.50μm^3/voxel shows a distinct increase to a percolation
419 radius of 0.38μm. At a resolution of 0.50μm^3/voxel the smallest connections (which control
420 flow in the models of higher resolution) have been lost, and as such the geometry and
421 topology of the system has been altered changing the connectivity of the pores. This
422 change in network properties is highlighted by the decrease in the number of nodes and
423 bonds from 0.40-0.50μm^3/voxel (Table 2). A change in the fluid flow properties of the

424 0.50μm^3/voxel model in comparison to the other resolution models could be expected.

425 ### 3.1.3. Porosity and Single-phase Permeability

426 All models had a target porosity of 26% and at each resolution a separate target porosity
427 trend (Figure 4a) had to be generated. The resultant model porosities fluctuate randomly
428 around 26% porosity, ranging from 26.8% porosity for the 0.10μm^3/voxel model down to
429 25.9% porosity for the 0.40μm^3/voxel model (Figure 8a). The model subvolumes (Table 1)
430 also show a narrow range of porosities indicating that a reasonably homogeneous medium
431 and representative elemental volume is being generated at all resolutions. The number of
432 crystals generated in each full size model is shown in Table 2.

433 Single-phase permeability (Figure 8b) shows limited variability across all models (between
434 1.8mD and 2.8mD), including for the 0.50μm^3/voxel model which displays no distinct
435 increase in permeability in comparison to the other resolutions. Additionally, there appears
436 to be a negative correlation between porosity and permeability due to changes in
437 resolution (Figure 8c); however over the range of porosities and permeabilities shown, the
438 variation in permeability is <1mD and in porosity is (<1.5%).

439 ### 3.1.4. Multi-phase Flow

440 Figure 9 shows the relative permeability curves from the multi-phase flow simulations over
441 the full 400^{3}voxel models at each resolution. These plots indicate the effective permeability
442 of the water and oil phases against saturation. The relative permeability curves of all
443 models are smooth indicating a homogeneous pore network at all resolutions.

444 The drainage curves for all models are similar (Figure 9a). Resolution (or average pore
445 size) can be seen to have little to no effect on water relative permeability, except for the
446 0.50μm^3/voxel resolution model which behaves slightly differently at mid-range saturations,
447 possibly reflecting the different connectivity and pore size distribution present. There is a
448 trend of decreasing oil relative permeability at the same saturation with a decrease in

449 resolution.

450 However, upon imbibition the models exhibit separate behaviour depending on their
451 resolution. For both wettability scenarios, the relative permeability curves for models of
452 resolution 0.10-0.40μm^3/voxel are indistinguishable while the relative permeability curves
453 of the 0.50μm^3/voxel models behave slightly differently. This is most pronounced for the
454 water relative permeabilities (Figure 9b&c) which show a higher relative permeability at the
455 same saturation in comparison to the higher resolution models. These differences in
456 relative permeability result in a residual oil which is dependent on resolution (and therefore
457 average pore size, Table 2) and is most clearly demonstrated by the capillary pressure
458 curves in Figure 10b,c. Under water wet imbibition (Figure 10b), the four higher resolution
459 models show an incremental variation in the residual oil saturation (fractional volume of oil
460 remaining in the model after full water flood), from 38% and 28%, while the residual oil
461 decreases notably more, to 23%, for the 0.50μm^3/voxel resolution model. Similarly,
462 although there is no incremental trend for the higher resolution models, under a fractionally
463 oil wet scenario (Figure 10c) the residual oil decreases substantially from around 24% to
464 15% for the model at 0.50μm^3/voxel resolution.

465 These results tend to suggest that the pore network of models generated at 0.50μm^3/voxel
466 resolution have sufficiently different properties (such as connectivity and pore size range
467 and distribution) such that the multi-phase fluid flow properties of these models is altered
468 in comparison to the higher resolution models.

469 ## 3.2 Effect of Total Microporosity and Micritic Dissolution

470 ### 3.2.1. Model Fabric Properties

471 Figure 11 shows 2D slices through a 3D realisation of each porosity model. Visually the
472 average pore size can be seen to increase with porosity, and the models appear to
473 represent a statistically homogeneous medium, with some random clustering of crystals as

474 is observed in SEM images.

475 The fabric of a rhombic micrite crystal model can be seen more clearly in Figure 12a and
476 Figure 12c which show the cubic/rhombic and euhedral micrite structure. Additionally
477 Figure 12 shows the effect of rounding on the crystal fabric. In Figure 12b & Figure 12d the
478 original grain structure is retained but without crystal vertices. Any apparently floating
479 grains are connected in the third dimension. The decrease in crystal size after micrite
480 rounding is demonstrated in Figure 12e.

481 ### 3.2.2. Pore Network Properties

482 Within the rhombic crystal models, average pore size increases with an increase in
483 porosity (Figure 11) which is supported by the results of the pore network extraction
484 analysis presented in Figure 13a. There is also an increase in the range of pore radii with
485 porosity although the range of pores captured in each model spans only one order of
486 magnitude and the majority of pores in the models have a radius of one voxel (two voxels
487 in diameter, Figure 13a). The homogeneity of the micritic fabric results in a narrow range of
488 pore radii reflecting a fairly homogeneous pore network distribution. The increase in
489 average pore size coincides with an increase in the average coordination number (Table 3)
490 while the total number of elements decreases for the models with the highest porosities.

491 The percolation radius increases with porosity (Figure 13c) which would be expected as
492 the average pore size increases. The 18% to 25% porosity models have a similar
493 percolation radius of 0.25μm, while the 30% and 35% porosity models show an increase to
494 0.35μm and 0.40μm respectively, indicating that larger pores are better connected in the
495 higher porosity models, which is again reflected in the average coordination number (Table
496 3).

497 In comparison to their rhombic crystal counterpart, the rounded micrite models exhibit an
498 increase in the range of pore sizes present and also an increase in the average pore

radius (Figure 13b), due to the decrease in crystal size (Figure 12e). Individually comparing a rhombic micrite model to its rounded counterpart demonstrates this trend clearly (Figure 13e).

The percolation radius increases after rounding for all models (Figure 13d & Figure 13f). However the average connection number does not show an increase across all models (Table 3). The increase in average connection number after rounding in comparison to before rounding is most pronounced for the low porosity models and this increase tapers off to become zero for the highest porosity models which exhibit no change in average connection number between the rhombic micrite to the rounded micrite fabrics. After rounding, all models have an average connection number of greater than 4.2.

3.2.3. Porosity and Single-Phase Permeability

The single-phase permeability and porosity results averaged over the individual results of the three realisations for each rhombic crystal model are shown in Figure 14a&b. For each set of realisations the three permeability values were within 0.01mD of the mean and the porosities were within 0.04% of the mean hence the variance was negligible. Over the range of porosities modelled there is an order of magnitude variation in the single-phase permeability, from 0.6mD to 7.5mD.

The effect of micrite rounding on porosity was slightly more pronounced for the lowest porosity models which exhibit an increase of 8% in porosity compared to a 7% increase for the models with the highest initial porosity (Figure 14b). The increase in porosity with rounding is reflected in the substantial increase in single-phase permeability for each individual model as shown by the dashed lines connecting the rhombic models to their rounded counterparts in (Figure 14b).

3.2.4. Multi-phase Flow

Based on the pore network properties of the original rhombic crystal models, the increase

524 in the average coordination number with increasing total porosity suggests that there
525 would also be a variation in the multi-phase flow properties for these models. However,
526 this expected trend is not observed (Figure 15a, b and c). During drainage (Figure 15a),
527 the oil relative permeability curves can be seen to depend on model porosity. Increasing
528 the porosity leads to a higher oil relative permeability at the same saturation, most likely
529 due to the presence of larger pores and due to the increase in connectivity with porosity.
530 Water relative permeabilities are however almost indistinguishable, showing only a small
531 variation between models and no discernable trend with porosity. An irreducible water
532 saturation of 0.07 is achieved for all models.

533 The imbibition curves for these models are indistinguishable (Figure 15b and c). There is,
534 however, a distinct difference between the residual oil saturation between the two
535 scenarios as water wet imbibition results in a residual oil saturation of 25% while the
536 fractionally wet scenario results in a residual oil saturation of 40%, which is more apparent
537 in the capillary pressure curves (Figure 16).

538 The results and trends for the rounded micrite models (Figure 15d,e,f) reflect the results of
539 the rhombic crystal model. Oil relative permeability curves during drainage show slightly
540 different behaviours dependent on total porosity whilst the imbibition curves are
541 indistinguishable. Moreover, the trends and curves for the two different crystal fabrics
542 cannot be distinguished from each other and so rounding the micrite crystals appears to
543 have little to no effect on multi-phase flow properties in comparison to the rhombic
544 counterpart.

545 ### 3.3 Effect of Mesoporosity within a Micritic Matrix

546 #### 3.3.1. Model Fabric Properties

547 The synthetic moldic mesopores modelled in this study were all located in the centre of
548 each octant within the grid. Therefore, as the mesopore radii are increased, the distance

separating the mesopores decreases (Figure 17, Table 4). The only model in which the mesopores touch and create a permeable pathway without microporosity is in the final model (Figure 17f) where mesopores have a radius of 45μm. This model is a purely synthetic, conceptual example to examine the change in behaviour upon introduction of a connected mesopore network. In all other models, the mesopores are generated such that they are separate bodies, including the model with mesopores of 40μm radius (Figure 17e) which have a minimum separation distance of a single grid voxel (Table 4). As such the connectivity between the mesopores in the models with mesopores of 40μm radius or less, is determined by the presence of microporosity, a shown in the cross-section through the 30μm radius model (Figure 17d). This style of connectivity is observed in epoxy resin cast images (Figure 1b) and additionally, the moldic mesopore in Figure 1b shows a rough topography around its perimeter which is caused by micrite. This rough topography is captured by the model, again, as shown in Figure 17d.

3.3.2. Pore Network Properties

As stated previously the mesopores in the first four models are very well connected by microporosity (Figure 17d), without which, they would otherwise be isolated. This variation in connectivity with mesopore separation (and size) is best examined using the average and maximum coordination numbers (Figure 18).

Upon introduction of the mesopores (10μm radius) to the micritic matrix, the average coordination number for each model increases and then progressively decreases with increasing mesopore radius (Figure 18a). The increase in average coordination number is because the 10μm radius mesopores connect to a large number of micropores initially. However, as the mesopores increase in size, there are more micropores connected to the mesopore edge (increase in maximum coordination number, Figure 18b) and each micropore that connects to a mesopore has, on average, half of the 3D possible

connections by connecting to a single mesopore rather than potentially being connected to multiple additional micropores, as those found in the centre of the micropore matrix do. Hence, the average coordination number decreases. However, the variation in average coordination for each matrix porosity is only 0.1. The average coordination number is calculated by frequency of occurrence and as such is dominated by the most common pore size, here, microporosity. Although pores with larger and larger coordination numbers are present as mesopore radii increases, the coordination number is still dominated by the microporosity whose presence decreases with increased mesopore radius.

As would be expected, the maximum coordination number for the models was found to decrease with increasing matrix porosity (Figure 18b) and increase with mesopore radius such that the maximum coordination number exceeded 1300 in the 40μm radii mesopore model with 18% matrix porosity (Figure 18b). The maximum coordination number decreases for 45μm radii mesopores because these pores are overlapping and as such are not entirely surrounded by microporosity, reducing the maximum coordination number.

3.3.3. Porosity and Single-phase Permeability

As mesopore radius increases, the relative proportion of the total porosity that is microporosity within the models decreases (Figure 19a) and as would be expected the overall effect of the presence of mesopores within a microporous matrix is to increase single-phase permeability (Figure 19b). However, lattice-Boltzmann flow simulations also indicate that the impact of the presence of mesopores on single-phase permeability varies depending on the porosity of the microporous matrix: a lower porosity matrix experiences a larger increase in single-phase permeability upon the introduction of mesopores into the model. While the mesopores are unconnected (up to a radius of 40μm), models with a matrix porosity of 18% experience a full order of magnitude increase in permeability while those with a higher matrix porosity experience an increase of less than an order of

599 magnitude.

600 Additionally, as the mesopore size increases, the variation in permeability with matrix
601 porosity also decreases, as indicated by the black boxes in Figure 19b: the spread of
602 permeabilities is lower for large mesopores than for smaller or no mesopores showing that
603 increasingly larger mesopores influence flow more relative to the matrix flow. Upon
604 connection of the mesopores at 45μm radius, all models see three orders of magnitude
605 increase in permeability as would be expected for a straight capillary tube. Due to the
606 larger capillary pressure required to simulate flow in the micropores compared to the
607 macropores, no such flow takes place, and as such, in these models flow completely
608 bypasses microporosity.

609 ### 3.3.4. Multi-phase Flow

610 From Figure 20 and Figure 21 it is clear that the presence of mesopores within the
611 microporous matrix, and indeed the different sizes of mesopores, greatly impact multi-
612 phase flow. The multi-phase flow properties can be seen to vary significantly across the
613 range of models generated.

614 Since the 45μm radii mesopore model is purely conceptual, its multi-phase flow results are
615 illustrated for drainage only to show the change in behaviour through connected
616 mesopores. For all other models during drainage, with increasing mesopore size (direction
617 of arrow) there is a decrease in oil relative permeability at the same saturation (the
618 opposite trend can be seen in the water relative permeability curves). This occurs because
619 the larger mesopores are filled with oil quicker than the smaller mesopores as they are
620 separated by thinner zones of micropores. When these mesopores are filled, the water
621 saturation decreases hugely, however there is still no permeable pathway from inlet to
622 outlet so the relative permeability of oil remains lower than in the smaller mesopore
623 models. This process is also linked to the trend that as mesopore radius increases, the

relative permeability curves become more step-like. This is best observed for the 30μm mesopore model water relative permeability curve (Figure 20g) and indicates a more heterogeneous pore system and the successive invasion of mesopores with oil. Sections of the curve with a much steeper gradient indicate slow drainage (a slower decrease in water saturation) as the oil is forced through the microporous horizons between mesopores. Sections of the curves with a much shallower gradient (boxes) indicate a sharp decrease in water saturation and the drainage of oil into a mesopore.

During water wet imbibition, these step wise relative permeability curves are not observed and this is related to trapping. During imbibition the smallest pores fill first which, due to the fabric of the models, results in a connected pathway from inlet to outlet through the micropores, bypassing the mesopores. As such, the oil filled mesopores become trapped, never being drained of their oil and the step wise saturation changes are not observed. This trapping effect results in an increase in residual oil with increasing mesopore size, where the volume of the pore system contained within the mesopores increases (Figure 22a). In other words, with an increase in homogeneity (more pores of a single type, here micropores, fewer mesopores) there is an improved sweep. Residual oil can also be seen to decrease with an increase in matrix porosity (Figure 21b,e,h and Figure 22).

The water-wet imbibition results for the models with 40μm radius mesopores, however, disregard this trend and this is thought to be because the pores are only disconnected from the outlet by a single row of voxels. As such, when merged with the microporous matrix, some of the mesopores then become directly connected to the outlet and are able to drain of oil, considerably decreasing residual oil saturation. This effect is interesting but it should be noted that such models are not representative elemental volumes as the number of unconnected mesopores may decrease to one, or even zero.

Under a fractionally oil wet imbibition scenario, quite the opposite trend can be observed.

With increasing mesopore radius, a decrease in residual oil occurs (Figure 21c,f,i and Figure 22b). As mentioned earlier, under a fractionally wet scenario the oil wettability is randomly distributed amongst 50% of the pores, independently of any of their physical properties (shape, size etc). As such, statistically, half of the mesopores will be oil wet allowing the development of oil films and oil drainage can continue from some mesopores even while water saturation is high. As mesopore size increases, the relative proportion of oil that can be drained through oil wet mesopores increases and so residual oil is lower for models with larger mesopores (Figure 21f&i). Of course, this is a statistical distribution of wettability and as such some models do not conform to this trend (e.g. Figure 21c, 30μm radii model).

4. Discussion

By investigating the effect of micropore size (Section 3.1) and total microporosity (Section 3.2) it has been shown that the new object based rock reconstruction algorithm used to model chalky microporous carbonate fabric is able to capture the basic textural properties that control the macro-scale single-phase permeability in these rock fabrics. There is a very good match between modelled single-phase permeability and the experimental porosity-permeability data (Figure 14a) reported for the chalky microporous facies of the Middle Eastern Lower Cretaceous Shuaiba formation (Fullmer et al., 2014). Additionally, the morphology of the modelled crystal fabrics are reasonable when compared to real rocks (Figure 5).The assumption that chalky micropores are so small that the capillary pressures are too high for oil to be have also proven incorrect by this study. The capillary pressure curves in Figures 10, 16 and 21 show ranges that are not out with the range expected within reservoirs.

We have aimed to represent some of the different fabrics of microporous carbonates by varying micropore size, total microporosity, crystal shape due to micritic dissolution and the

674 presence of mesopores within the matrix, all of which can be observed in nature through
675 sample analysis. Since modelling chalky micropores requires sub-micron resolution, being
676 able to either observe or represent the micropores within a multiscale network is a
677 formidable challenge. Indeed, in all digital rock reconstructions there is a trade-off between
678 the spatial resolution of the model and the largest (or smallest) scale of features that can
679 be examined. The upper limits of computational power and memory restrict firstly the
680 number of voxels in a model volume and therefore the physical volume of a model that can
681 be created, and secondly restrict the grid volume through which fluid flow can be
682 simulated. As such, while a higher spatial resolution of model allows features to be more
683 finely resolved, a higher resolution significantly reduces the physical model size that can
684 be held within the memory limits of the machine being used since the 3D model size
685 increases as the cube of the number of voxels along each axis.

686 While examining the effect of micropore size it has been observed that the micropores in
687 models generated between 0.10-0.40μm^3/voxel resolution have very similar single- and
688 multi-phase flow behaviour. This result suggest that models generated at a resolution of
689 0.40μm^3/voxel are able to represent the same physical pore scale flow as models
690 generated at 0.10μm^3/voxel, a resolution which is much closer to the size of chalky
691 micropores observed in epoxy resin casts (Figure 1b). Indeed, the single-phase
692 permeability match with experimental data reported in Section 3.2 further corroborates that
693 modelling the microporous fabrics at a resolution of 0.40μm^3/voxel captures the relevant
694 pore scale features that exist within real chalky microporous carbonate fabrics.

695 However, models generated at a resolution of 0.50μm^3/voxel exhibited different pore
696 network and multi-phase fluid flow properties. In comparison to these at higher resolutions
697 models at 0.50μm^3/voxel showed a larger percolation radius (Figure 7) and quite different
698 water relative permeability behaviour during imbibition (Figure 9), which resulted in a lower
699 residual oil saturation (Figure 10). It is difficult to determine the exact reasons for this

700 change in residual oil, however it is likely to be due to the larger volume of the pore
701 network contained in the modal pore size within this model and also due to the increased
702 percolation threshold which will reduce trapping. These results tend to suggest that a
703 tipping point in the multi-phase flow properties of micropores falls between those with a
704 modal size range of between 0.40μm^3/voxel and 0.50μm^3/voxel. Below 0.40μm^3/voxel the
705 multi-phase flow properties are similar while above 0.40μm^3/voxel, the multi-phase flow
706 properties vary quite significantly. Interestingly though, the 0.50μm^3/voxel resolution model
707 did not exhibit a distinct increase in single-phase permeability, and all of the different
708 resolution models have very similar single-phase permeability properties (Figure 8). The
709 distinct change in percolation threshold and connectivity of the 0.50μm^3/voxel model
710 (Figure 7) has little effect on single-phase permeability in comparison to the other
711 resolution models.

712 These results provide the ability to model larger physical volumes, and to incorporate
713 chalky microporosity into a more multiscale network, by modelling at a resolution of
714 0.40μm^3/voxel. At this resolution it was shown that volume of microporosity affects single-
715 phase permeability by an order of magnitude (0.6mD to 7.5mD) over the range of
716 porosities examined (18-35%, Figure 14) but that increasing matrix porosity has very little
717 effect on multi-phase relative permeability and residual oil saturation under both the
718 strongly water wet and fractionally wet wettability scenarios (Figure 15). The effect of
719 micrite rounding due to dissolution has also been examined here. Comparing a rhombic
720 matrix to its rounded counterpart (dashed lines, Figure 14b) shows an increase in porosity
721 of 7-8% (which is in agreement with the increase in porosity due to rounding reported by
722 Lambert et al. (2006)) and also a substantial increase in single-phase permeability, up to
723 an order of magnitude for the lowest porosity models. As such, if a reservoir was of
724 constant volume microporosity within the rhombic fabrics, rounding of the original fabric
725 (most probably toward the top of the oil column) would result in a stratigraphic alteration of

726 the single-phase permeability due to the increase in porosity, as indicated by these results
727 and in agreement with Lambert et al. (2006). It is interesting to note, however, that the
728 overall effect of micritic dissolution on the single-phase and multi-phase permeability
729 trends appears to be limited. At approximately the same porosity (30%, indicated by the
730 arrows in Figure 14b), the permeability in a rounded micrite model can be seen to be only
731 slightly higher (~1mD) than in a rhombic crystal model. This is also shown in the multi-
732 phase flow results (Figure 15) which indicate that micrite dissolution and rounding has very
733 little effect on multi-phase flow under these wettability scenarios. It appears that rounding
734 the micrite crystals has little to no effect on the pore network topology in comparison to the
735 pore networks within rhombic micrite and hence little change in the multiphase flow
736 properties.

737 At a resolution of 0.40μm^3/voxel it is possible to include up to three orders of magnitude of
738 pore size variation through the inclusion of meso-scale pores (>10μm diameter). Results
739 have shown that the addition of mesopores to a micritic matrix greatly impacts the
740 geometry and topology of the pore system (Figure 18) and the single-phase permeability
741 of the models increases with increasing mesopore radius (Figure 19). The relationship
742 between single-phase permeability and mesopore radius is non-linear but is related to the
743 separation distance between the mesopores and therefore the proportion of microporosity
744 within the models. Here microporosity dominates single-phase permeability where it
745 provides the only permeable connection between mesopores (mesopores with a radius of
746 10-30μm) and single-phase permeability is limited to less than 20mD. A distinct increase in
747 single-phase permeability for models with mesopores of 40μm radii is due to the single
748 voxel separation between the mesopores: at such small separation distances the
749 mesopores may be connected by a single or a few micropores and as such the
750 permeability becomes dominated by the mesopores. This is the same for models with
751 mesopores of 45μm radius, where the flow is able to completely bypass the microporosity

752 and permeability thus increases by three orders of magnitude.

753 The multi-phase flow properties of the models also vary significantly with both mesopore
754 size and matrix porosity and it has been shown that these results are again related to the
755 separation distance between mesopores and the relative proportion of microporosity in the
756 models. Most importantly, under a water wet imbibition scenario, an increase in
757 homogeneity (more micropores, fewer mesopores) increases the sweep of the model
758 (Figure 22a). This increase in sweep with homogeneity has been reported by other authors
759 in fabrics where micropores are present (Hollis et al., 2011; Fullmer et al., 2014) and is
760 also observed in the water wet imbibition capillary pressure curves in Figure 21b, e & h.

761 We are aware that in reality not all mesopores in a reservoir have the same shape and
762 size. Here, the mesopore models are entirely synthetic and the porosities of the models
763 with the largest mesopores are beyond the porosities typically observed in these types of
764 carbonates (Figure 19a). Yet this study has demonstrated the flexibility of the developed
765 algorithm to explore these variations and provides a basis to further develop future studies.
766 By methodologically altering certain parameters of the porous fabrics (crystal packing,
767 crystal size, porosity, mesopores) and also the properties of fluids simulated, it will be
768 possible to build a state-space of how the properties of microporous carbonates vary
769 under these different fabrics and use the trends to predict single-phase and multi-phase
770 flow.

771 Finally, across all different fabrics it has been shown that the wettability scenario modelled
772 during imbibition impacts the residual oil. The wetting state of any rock is extremely hard to
773 determine as core wettability experiments are expensive (both in time and money), and
774 more importantly it is difficult to ensure that the core wettability under lab conditions is the
775 same as in-situ subsurface conditions. Relative permeability data are therefore difficult to
776 acquire under reservoir conditions. If such data are available, they are usually only for one

777 particular bulk plug sample while the wetting state of a carbonate may vary at a much
778 smaller (pore scale) and indeed larger scales. Modelling two phase flow under a variety of
779 different wettability scenarios is one possible way to understand how the fluid flow
780 properties would vary under different wetting states and this wettability dependent variation
781 in multi-phase flow properties and residual oil has been demonstrated in this study by
782 looking at strongly wet imbibition and fractionally oil wet imbibition. The multi-phase flow
783 results for models with varying sizes of mesopores demonstrates the dependency of
784 recovery on wetting scenario (Figure 22).

785 However, the wetting state of a real rock is not randomly distributed throughout the pore
786 network as is simulated for the fractionally wet wettability case here. Intermediate
787 wettability (where part of the pore system is oil-wet and the remainder oil-wet) maybe
788 controlled by the pore size or pore shape (degree of curvature), or wettability is controlled
789 by mineralogy (Kovscek et al., 1993; Skauge at al., 2004). The mineralogy of the micrite in
790 these microporous carbonate models does not vary, and as such mineralogy does not
791 need to be considered as a controlling factor on wettability alteration. Pore size and shape,
792 however, are viable controls on wettability at the pore scale. While network models are
793 able to determine wetting alteration due to pore size, they are not able to model wettability
794 alteration due to changes in pore shape/curvature as defined by the extracted pore
795 network. Blunt (1998) introduced a model capable of modelling wettability based on pore
796 shape parametrically but a network model flow simulator capable of modelling fluid layers
797 that are dependent on pore shape as defined in the pore network, is vital if we are to be
798 able to predict multi-phase flow properties of carbonates and indeed, other media. Under a
799 wetting state controlled by pore shape, the multi-phase properties of rounded micrite
800 compared to rhombic micrite may indeed be very different as although the structure of the
801 pore network has been seen to vary only slightly in this study, the largest effect of micrite
802 rounding could be on pore shape.

5. Conclusions

We present a flexible object-based rock reconstruction algorithm that reproduces the fabric of chalky microporous carbonates. We apply the algorithm to probe the effects of micropore size, total microporosity and micritic dissolution on both single- and multi-phase fluid flow properties within a purely micritic matrix. The algorithm is also used to examine the effect of the presence of mesopores of varying sizes within a micritic matrix on both single- and multi-phase flow.

Micropore size (controlled by varying model resolution) was found to have little to no effect on single-phase permeability within the range of resolutions modelled here (0.10-0.50μm^3/voxel). However a tipping point in the multi-phase flow properties has been observed for microporous fabrics with pores no smaller than 0.50μm^3, which exhibit quite different flow properties to those with smaller sizes. We conclude that voxels and pores at least as small as 0.40μm^3 for such modelling.

Total microporosity has been shown to influence single-phase permeability significantly and over the range of porosities modelled (18-35%) an order of magnitude increase on permeability occurs. These results indicate that microporosity can conduct significant single-phase permeabilities of up to 7.5mD which is in agreement with literature reported experimental data. Total microporosity was however shown to have little to no effect on multi-phase flow behaviour and oil recovery in these models.

The algorithm is capable of mimicking micritic dissolution (rounding) and results indicate that rounded micritic fabrics have a considerable effect on the porosity (increase of up to 8%) and single-phase permeability (increase of up to order of magnitude) in comparison to their original rhombic micritic fabrics, while the overall porosity-permeability trends exhibit only slight increase in permeability at a given porosity suggesting that the pore network topology is not significantly altered by rounding. Additionally, multi-phase flow properties

828 remain unaltered between the rhombic crystal fabric and the rounded model fabric.

829 Finally it has been shown that the presence of mesopores within a micritic matrix can
830 greatly impact flow properties after they become directly connected, but if they are
831 disconnected single-phase permeability is controlled by micropores and only an order of
832 magnitude variation in permeability is observed with varying microporosity. Indeed, these
833 fabrics have been shown to be able to conduct significant permeabilities of up to 20mD
834 while the mesopores are unconnected, demonstrating that microporosity cannot simply be
835 overlooked within multiscale carbonate pore systems. Additionally, it has been shown that
836 fabrics with a higher fraction of total porosity that is microporosity retain a much lower
837 residual oil saturation during water wet imbibition. Under this wettability scenario, the
838 presence of microporosity within a carbonate reservoir is desirable, as it increases the
839 sweep of the reservoir during imbibition.

840 Carbonate microporosity is found within many different rock fabrics and often in
841 combination with other scales of porosity. This study has examined only a small sector of
842 the spectrum of fabric variation and indeed the different hypothetical wettability scenarios,
843 but has shown the breadth of single-phase flow properties and more importantly multi-
844 phase flow properties that can occur through these fabrics. When assessing the
845 producibility of microporous carbonates it is therefore important to consider the
846 microporosity and understand its role in fluid flow through the fabrics present. The
847 algorithm developed here provides a flexible platform with which to probe the full spectrum
848 of variations of microporous fabrics and different geologically controlled wettability
849 scenarios.

850 **References**

851 Al-Kharusi, A.S., and Blunt, M.J., 2008, Multi-phase flow predictions from carbonate pore
852 space images using extracted network models, Water Resources Research, V.44

853 Bakke. S., and Øren. P-E., 1997, 3-D Pore-Scale Modelling of Sandstones and Flow
854 Simulations in the Pore Networks, SPE Journal, v. 2.

855 Biswal. B., Øren. P-E., Held. R., Bakke. S., and Hilfer. R., 2007, Stochastic multiscale
856 model for carbonate rocks, Physical Review E 75, 061303.

857 Biswal. B., Held. R.J., Khanna. V., Wang. J., and Hilfer. R., 2009a, Towards precise
858 prediction of transport properties from synthetic computer tomography of reconstructed
859 porous media, Physical Review E 80, 041301.

860 Biswal. B., P-E Øren., Held. R., Bakke. S., and Hilfer. R, 2009b, Modelling of multiscale
861 porous media, Image Analysis and Stereology 28, p23-34.

862 Blunt, M., 1998, Physically-based network modelling of multiphase flow in intermediate-wet
863 porous media, Journal of Petroleum Science and Engineering, 20, p117-125

864 Bobek, J. E., Mattax, C. C., and Denekas, M. O., 1958, Reservoir Rock Wettability - Its
865 Significance and Evaluation, Society of Petroleum Engineers.

866 Budd, D., 1989, Micro-rhombic calcite and microporosity in limestones: a geochemical
867 study of the lower cretaceous Thamama group, UAE, Sedimentary Geology, v. 633-4,
868 p293-311.

869 Cantrell, D. L. and Hagerty, R. M., 1999, Microporosity in Arab formation carbonates,
870 Saudi Arabia, GeoArabia 4, p129 - 154.

871 Chilingar, G.V. and Yen, T. F., 1983, Some Notes on Wettability and Relative Permeabilities
872 of Carbonate Reservoir Rocks, II, Energy Sources, Vol. 7.

873 Choquette, P., and Pray, L., 1970, Geologic Nomenclature and Classification of Porosity in
874 Sedimentary Carbonates, AAPG Bulletin, v. 542, p207-250

875 Chun, B. and Ladd, A. J. C., 2007, Interpolated boundary condition for lattice Boltzmann
876 simulations of flows in narrow gaps, Phys. Rev. E 75

877 Cox, P., Wood, R., Dickson, J.A.D., Al-Rougha, H.B., Shebl, H., and Corbett, P.W.M., 2010,
878 Cynamics of cementation in response to oil charge: Evidence from a Cretaceous
879 carbonate field, U.A.E., Sedimentary Geology, v228(3-4), p246-254

880 Cuiec, L., 1984, Rock/crude-oil interactions and wettability: An attempt to understand their
881 interrelation, Society of Petroleum Engineers, Vol. 13211

882 Darcy, H., 1856, Les Fontaines Publiques de la Ville de Dijon, Dalmont, Paris

883 Desplat, J. C., Pagonabarraga, I., and Bladon, P., 2001, LUDWIG: A parallel Lattice-
884 Boltzmann code for complex fluids, Computer Physics Communications, v. 1343. p273-
885 290

886 Deville de Periere, M., Durlet, C., Vennin, E., Lambert, L., Bourillot, R., Caline, B., and Poli,
887 E., 2011, Morphometry of micrite particles in cretaceous microporous limestones of the
888 Middle East: Influence on reservoir properties, Marine and Petroleum Geology, 289,
889 p1727-1750.

890 Dravis, J.J., 1989, Deep-burial microporosity in upper Jurassic Haynesville oolitic
891 grainstones, East Texas, Sedimentary Geology, Volume 63, Issues 3–4, Pages 325-341.

892 Folk, R. L., 1962, Classification of carbonate rocks, AAPG memoirs, 1, p62-84.

893 Fullmer, S. M., Guidry, S. A., Gournay, J., Bowlin, E., Ottinger, G., Al Neyadi, A. M., and
894 Edwards, E., 2014, Microporosity: Characterization, Distribution, and Influence on Oil
895 Recovery, International Petroleum Technology Conference Abstract.

896 Heasley, E.C., Worden, R.H., and Hendry, J.P., 2000, Cement distribution in a carbonate
897 reservoir: recognition of a palaeo oil–water contact and its relationship to reservoir quality
898 in the Humbly Grove field, onshore, UK, Marine and Petroleum Geology, Volume 17, Issue
899 5, p639-654

900 Hollis, C., Vahrenkamp, V., Tull. S., Mookerjee. A., Taberner. C., and Huang. Y., 2011, Pore

system characterization in heterogeneous carbonates: An alternative approach to widely-used rock-typing methodologies, Petroleum Geoscience 27, p772-793.

Jiang, Z., Wu, K., Couples, G.D., van Dijke, M.I.J., and Sorbie, K.S., 2007, Efficient extraction of networks from 3D porous media, Water Resource Research, 43, W12S03.

Kashfi, M., 1974, A Brief Study of Reservoir Rock Wettability in the Iranian Oil Fields, Energy Sources, Vol. 1

Kirkham, A., Bin Juma, M., McKean, T.A.M., Palmer, A.F., Smith, M.J., Thomas, A.H., and Twombley, B. N., 1996, Fluid saturation prediction in the 'transition zone' carbonate reservoir, Abu Dhabi, Geoarabia 1, p551-566

Kovscek, A.R., Wong, H., and Radke, C.J., 1993, A pore-level scenario for the development of mixed wettability in oil reservoirs, AIChE Journal, 39(6), p1072-1085

Lambert, L., Durlet, C., Loreau, J.-P. and Marnier, G., 2006, Burial dissolution of micrite in Middle East carbonate reservoirs Jurassic-Cretaceous: keys for recognition and timing, Marine and Petroleum Geology 231, p79-92.

Lucia, F.J. and Loucks, R.G., 2013, Micropores in carbonate mud: early development and petrophysics, GCAGS Journal, Volume 2, p1-10

Morrow, N. R., 1976, Capillary Pressure Correlations for Uniformly Wetted Porous Media, Petroleum Society of Canada

Moshier, S., 1989a, Development of microporosity in a micritic limestone reservoir, lower cretaceous, Middle East, Sedimentary Geology 633-4, p217-240

Moshier, S. O., 1989b, Microporosity in micritic limestones: a review, Sedimentary Geology 63, p191-213.

Okabe, H., and Blunt, M., 2004, Prediction of permeability for porous media reconstructed using multiple-point statistics, Physical Review E, 70, 066135

925 Øren. P-E., Bakke. S., and Arntzen, O., 1998, Extending predicative capabilities to network
926 models, SPE Journal 3, 324-336

927 Øren. P-E. and Bakke. S., 2003, Reconstruction of Berea sandstone and pore-scale
928 modelling of wettability effects, Journal of Petroleum Science and Engineering 39, p177–
929 199

930 Pittman, E. D., 1971, Microporosity in Carbonate Rocks: geological notes, AAPG Bulletin,
931 5510, p1873-1878.

932 Richard, J., Sizun, J.P., and Machhour, L., 2007, Development and compartmentalisation
933 of chalky carbonate reservoirs: The Urgonian Jura-Bas Dauphine platform model
934 (Genissiat southeastern France), Sedimentary Geology, 198, p195-207

935 Roth. S., Biswal. B., Afshar. G., Held. R., Øren. P-E., Berge. L., and Hilfer. R., 2011,
936 Continuum-based rock model of a reservoir dolostone with four orders of magnitude in
937 pore sizes, AAPG Bulletin, 956, p925-940.

938 Schneider, C.A., Rasband, W.S., and Eliceiri, K.W., 2012, NIH Image to ImageJ: 25 years
939 of image analysis, Nature Methods 9, p671-675.

940 Smith, L. B., Eberli, G. P., Masaferro, J. L., & Al-Dhahab, S., 2003, Discrimination of
941 effective from ineffective porosity in heterogeneous Cretaceous carbonates, Al Ghubar
942 field, Oman, AAPG bulletin, 879, p1509-1529.

943 Sengupta. A., Hammond, P., Frenkel, P., and Boek, E., 2012, Error analysis and correction
944 for Lattice Boltzmann simulated flow conductance in capillaries of different shapes and
945 alignments, Journal of Computational Physics, 231, p2634–2640.

946 Skauge, A., Spildo, K., HØiland, L., Vik, B., and Ottesen, B., 2004, Experimental evidence
947 of different intermediate wetting states, Society of Core Analysts Paper, SCA2004-04

948 Skauge, A., Sorvik, A., Vik, B., and Spildo, K., 2006, Effect of wettability on oil recovery

949 from carbonate material representing different pore classes, Society of Core Analysts
950 Paper, SCA2006-01

951 Torquato, S., 1984, Bulk properties of two-phase disordered media, I. Cluster expansion
952 for the effective dielectric constant of dispersions of penetrable spheres, J Chem Phys 81.
953 5079-5088.

954 Torquato, S., 1985, Bulk properties of two-phase disordered media. II. Effective
955 conductivity of a dilute dispersion of penetrable spheres. J Chem Phys 83, 4776-4785.

956 Torquato, S., 1986, Bulk properties of two-phase disordered media, ill. New bounds 98 on
957 the effective conductivity of dispersions of penetrable spheres, J Chem Phys 84.6345-
958 6359.

959 Treiber, L. E., and Owens, W. W., 1972, A Laboratory Evaluation of the Wettability of Fifty
960 Oil-Producing Reservoirs, Society of Petroleum Engineers

961 Valvatne, P. H., and Blunt, M. J., 2004, Predictive pore-scale modelling of two-phase flow
962 in mixed wet media, Water Resources Research, 407.

963 Van Geet, M., Swennen, R., and Wevers, M., 2000, Quantitative analysis of reservoir rocks
964 by microfocus X-ray computerised tomography, Sedimentary Geology, Volume 132, Issues
965 1–2, Pages 25-36

966 Vogel, H.-J., and Roth, K., 2001, Quantitative morphology and network representation of
967 soil pore structure, Advances in Water Resources, Volume 24, Issues 3–4, Pages 233-242.

968 Volery, C., Davaud, D., Foubert, A., and Caline, B., 2009, Shallow-marine microporous
969 carbonate reservoir rocks in the Middle East: Relationship with seawater Mg/Ca Ratio and
970 eustatic sea level, Journal of Petroleum Geology, Vol.32(4), p313-326

971 Volery, C., Davaud, E., Durlet, C., Clavel, B., Charollais, J., and Caline, B., 2010,
972 Microporous and tight limestones in the Urgonian Formation (late Hauterivian to early

973 Aptian) of the French Jura Mountains: Focus on the factors controlling the formation of
974 microporous facies, Sedimentary Geology, Volume 230

975 Wagner, O., 1990, Geochemical stratigraphy and porosity controls in Cretaceous
976 carbonates ear the Oman mountains, Geological Society, London, Special Publications,
977 $9(1), p127-137

978 Wu, K., Nunan, N., Crawford, J., Young, I., and Ritz, K., 2004, An efficient Markov chain
979 model for the simulation of heterogeneous soil structure, Soil Science Society of America
980 Journal, 68(2), p346

981 Wu, K., van Dijke, M., Couples, G., Jiang, Z., Ma, J., Sorbie, K., Crawford, J., Young, I.,
982 and Zhang, X, 2006, 3D stochastic modelling of heterogeneous porous media applications
983 to reservoir rocks, Transport in Porous Media, v65, p443-476

984 Wu, K., Ryazanov, A., van Dijke, M., Jiang, Z., Ma, J., Couples, G., and Sorbie, K., 2008,
985 Validation of methods for multi-scale pore space reconstruction and their use in prediction
986 of flow properties in carbonate, Society of Core Analysts Paper, SCA 2008-34

Figure 1 Secondary electron SEM images of chalky microporous carbonates. (a) Image of a rough cut chip showing the rhomboidal shape of micrite crystals. (b) Epoxy resin cast showing the sponge like network of microporosity and its connectivity with a larger, meso-scale pore. The inset shows a high resolution image of the plate-like morphology of chalky microporosity between the facets of three micrite crystals. (c) Image of a rough cut chip showing the rounding effect of micritic dissolution: the example highlighted crystals exhibit no vertices or facets.

Figure 2 Example Backscatter SEM images of chalky carbonate microporosity that can be used to extract quantitative data for model calibration. (a) & (b) Typical backscatter SEM images used for crystal diameter measurements. (c) Crystal size distribution as measured from backscatter images and used to populate models at a voxel resolution of 0.4μm^3/voxel.

Figure 3 (a) 100x100voxel slice through a 25% porosity model demonstrating the crystal overlap created by crystal layering. Edge voxels (white) can be seen to overlap or touch one another while individual crystal centres (grey) are entirely separate. (b) Binarised final fabric of the same slice. (c) and (d) show example layered crystal structures of two sizes used in the algorithm (with front-right section removed to show internal layered structure).

Figure 4 Example data from sensitivity tests calculating solid volume loss due to crystal overlap. (a) Sensitivity test data and resultant trend for 400^3 models at a resolution of 0.4μm^3/voxel over a range of porosities. Using the trend it is possible to calculate the model target porosity (ϕ) that should be used in order to achieve any particular required final porosity (ϕ_D). The arrow shows that a target of ϕ=18% should be used to obtain a final porosity ϕ_D=25% (c) These sensitivity tests can be performed for any grid size (three examples are shown) and at any resolution.

Figure 5 Visual comparison between (a) micritic fabrics in a secondary electron SEM image of a rough cut chip and (b) a 300x300voxel slice of a 0.10μm^3/voxel resolution model viewed in pseudo-3D.

Figure 6 400x400 slice of a model at each resolution scaled to relative physical size. 0.50μm^3/voxel through to 0.10μm^3/voxel in (a) through (e) respectively. All models have ~26% porosity.

Figure 7 Pore network properties of different resolution models. Key indicates the voxel resolution of each model. (a) Pore radius distribution. (b) Euler number connectivity function.

Figure 8 (a) Porosities computed from subvolumes at each resolution. (b) Single-

phase permeabilities computed from subvolumes at each resolution. (c) Porosity plotted against single-phase permeability computed for each subvolume (unfilled symbols) and full scale volume realisation (filled symbols).

Figure 9 Relative permeability curves from simulations of multi-phase flow on extracted pore networks within models of varying resolution. Water relative permeability curves are shown as solid lines, oil relative permeability curves are shown as dashed lines. WW= water wet wettability & FW= fractionally wet wettability.

Figure 10 Capillary pressure cures from simulation of multi-phase flow on extracted networks within models of varying resolution.

Figure 11 An example 2D slice through a single realisation of each 3D porosity model. Panels a to e show models of 18% to 35% porosity respectively (refer to Table 3 for exact porosity values). Black voxels indicate pores, while white voxels indicate solid. All slices have dimensions of 400x400 voxels and a resolution of 0.40μm^3/voxel.

Figure 12 A comparison of model fabrics before and after micrite rounding for the 25% porosity model. (a) 100^3 voxel volume of the rhombic crystal model. (b) 100^3 voxel of the rounded crystal model. (c) 100x100 voxel slice of the rhombic crystal model. (d) 100x100 voxel slice of the rounded crystal model. (e) Crystal diameter histogram and cumulative frequency plots for a 400x400 voxel slice of the rhombic and rounded models.

Figure 13 Pore network properties of rhombic models and rounded models. Upper row shows pore radius distributions and lower row shows Euler number connectivity functions. Left hand column shows results for rhombic models, central column shows results for rounded micrite models, and right hand figures show a comparison between the results for 25% porosity rhombic micrite and its resultant rounded micrite fabric counterpart. Keys shown apply to figures directly them.

Figure 14 Porosity against single-phase permeability plots. (a) Rhombic crystal model results plotted with data from Fuller et al. (2014). Modelled fabrics represent those termed Type I by the Fuller et al. scheme. Model data points are an average over three realisations of each model. (b) Comparison between rhombic crystal and rounded crystal porosity-permeability results. Dashed lines trace the transition of the porosity-permeability measurement from the original, rhombic crystal model to its rounded counterpart. Arrows indicate a rhombic crystal model and a rounded crystal model with similar porosities (~30%).

Figure 15 Relative permeability curves from simulations of multi-phase flow on extracted pore networks. Upper row shows results for rhombic crystal models, lower row shows results for rounded crystal models. Water relative permeability curves are shown as solid lines, oil relative permeability curves are shown as dashed lines.

Figure 16 Capillary pressure curves from simulation of multi-phase flow on extracted pore networks. Upper row shows results for rhombic crystal models, lower row shows results for rounded crystal models.

Figure 17 (a) to (c), (e) & (f) show the synthetic moldic mesopore configurations used. (d) Shows a slice through model (c) as indicated by the dashed line in (c) after the mesopores have been combined with 25% matrix porosity model.

Figure 18 Coordination number data for mesopore models. (a) Average coordination number. (b) Maximum coordination number.

Figure 19 Porosity and single-phase permeability plots. (a) Microporosity as a proportion of total porosity. Shading indicates mesopore radii as shown on the plot. (b) Mesopore radius plotted against single-phase permeability. The 0μm radius mesopore (x-axis) data points indicate purely micritic matrix. Boxes highlight the decrease in range of permeabilities with matrix porosity as mesopore radius increases.

Figure 20 Multi-phase flow relative permeability curves for models with varying mesopore radii (see key) and varying matrix porosity. Upper, middle and lower rows indicate models of 18%, 25% and 35% matrix porosity respectively. Arrows indicate direction of increasing mesopore radius for the oil relative permeabilities (dashed lines). Water relative permeabilities are indicated as solid lines. Boxes in (g) indicate fast water drainage in comparison to the slower drainage through steeper curve gradients either side.

Figure 21 Capillary pressure curves for models with varying mesopore radii (see key) and varying matrix porosity. Upper, middle, lower rows indicate models of 18%, 25% and 35% matrix porosity respectively. Arrows indicate direction of increasing mesopore radius.

Figure 22 Plots of mesopore size against residual oil saturation for (a) water wet imbibition and (b) fractionally wet imbibition, under varying matrix microporosity. The direction of arrows indicates direction of decreasing proportion of microporosity.

Table 1 Model resolutions, physical size of full model and number of voxels in each subvolume model.

Table 2 Number of crystals, nodes and bonds, and average pore radius generated at each resolution.

Table 3 Pore network statistics for rhombic crystal models of different porosities and corresponding rounded crystal model (indicated by a and b).

Table 4 Model mesopore radius and corresponding mesopore separation distances.

Resolution (μm^3/voxel)	Full Model Physical Size (μm^3)	Subvolume Model Size (voxels)
0.10	40^3	---
0.20	80^3	200^3
0.30	120^3	133^3
0.40	160^3	100^3
0.50	200^3	80^3

Model Resolution (μm^3/voxel)	# Crystals	Average Pore Radius (μm)	# Nodes	# Bonds
0.10	6417	0.26	19270	10491
0.20	39858	0.30	133954	68037
0.30	116407	0.37	283997	141547
0.40	271875	0.38	709514	342223
0.50	495190	0.44	584850	187095

	Model	Porosity %	# Pores	# Throats	# Elements	Average Coordination #	Average Pore Radius (μm)
Rhombic	1a	18.9	303255	576183	879438	3.78	0.329
	2a	21.3	323128	633370	956498	3.91	0.327
	3a	25.6	332709	683879	1016588	4.09	0.336
	4a	30.6	309397	663326	972723	4.27	0.344
	5a	35.7	268670	594955	863625	4.41	0.421
Rounded	1b	27.1	293660	623913	917573	4.23	0.327
	2b	29.6	282337	608558	890895	4.29	0.438
	3b	33.7	249887	547965	797852	4.36	0.543
	4b	38.3	207306	460690	667996	4.42	0.615
	5b	42.9	165973	369289	535262	4.42	0.668

Mesopore Radius (μm)	Minimum Separation (voxels)
10	150
20	100
30	50
40	1
45	0

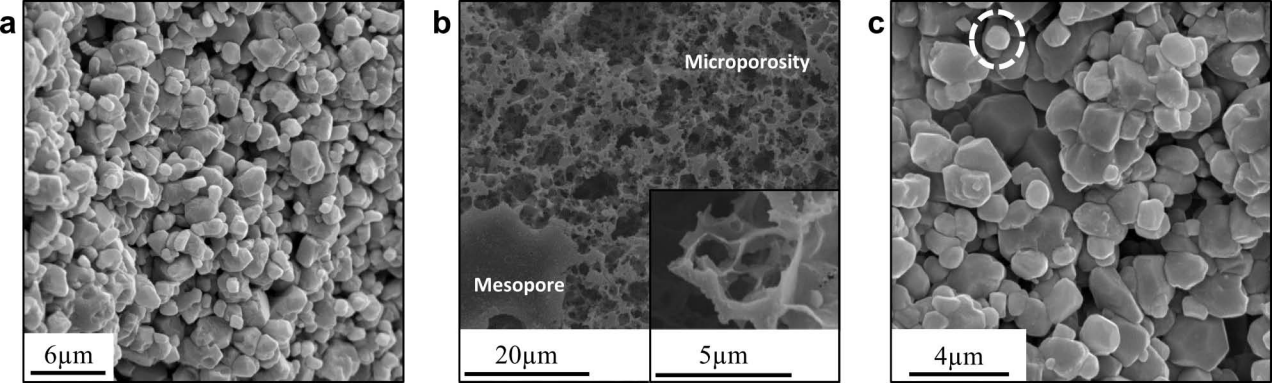
a
6μm
b
Microporosity
Mesopore
20μm
5μm
c
4μm

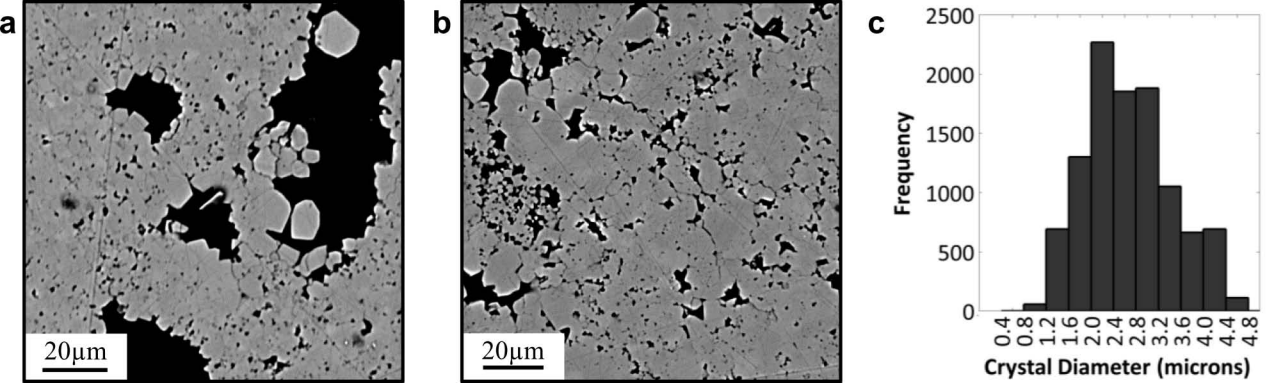
a
20μm
b
20μm
c
2500
2000
1500
1000
500
0
Frequency
0.4
0.8
1.2
1.6
2.0
2.4
2.8
3.2
3.6
4.0
4.4
4.8
Crystal Diameter (microns)

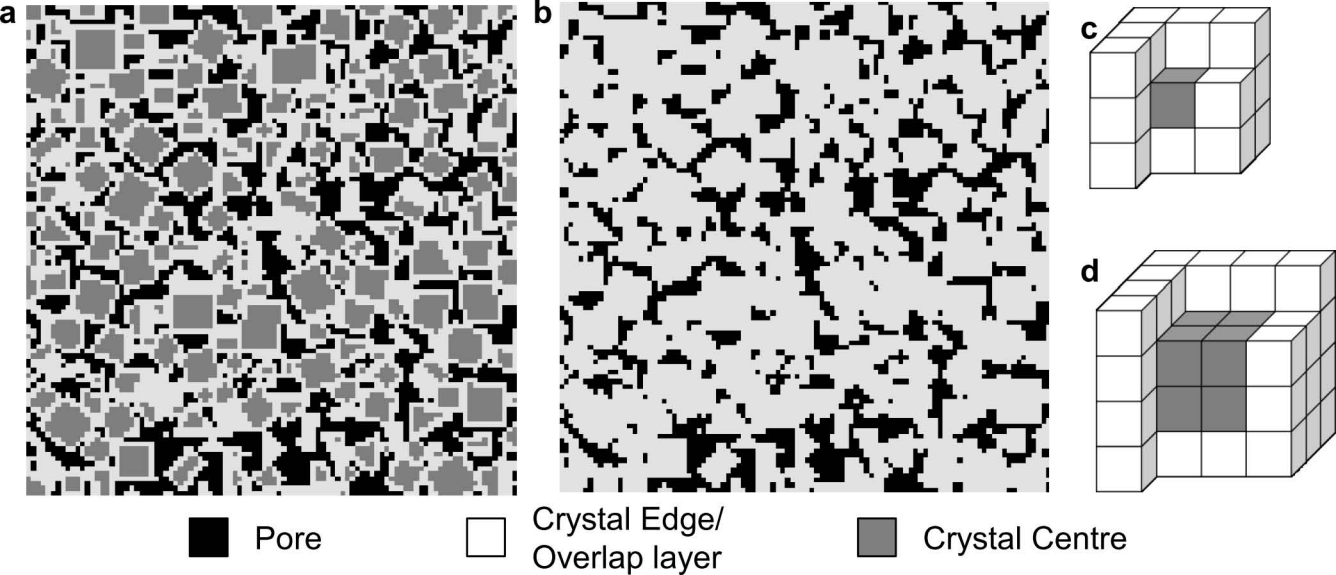
a
b
c
d
Pore
Crystal Edge/
Overlap layer
Crystal Centre

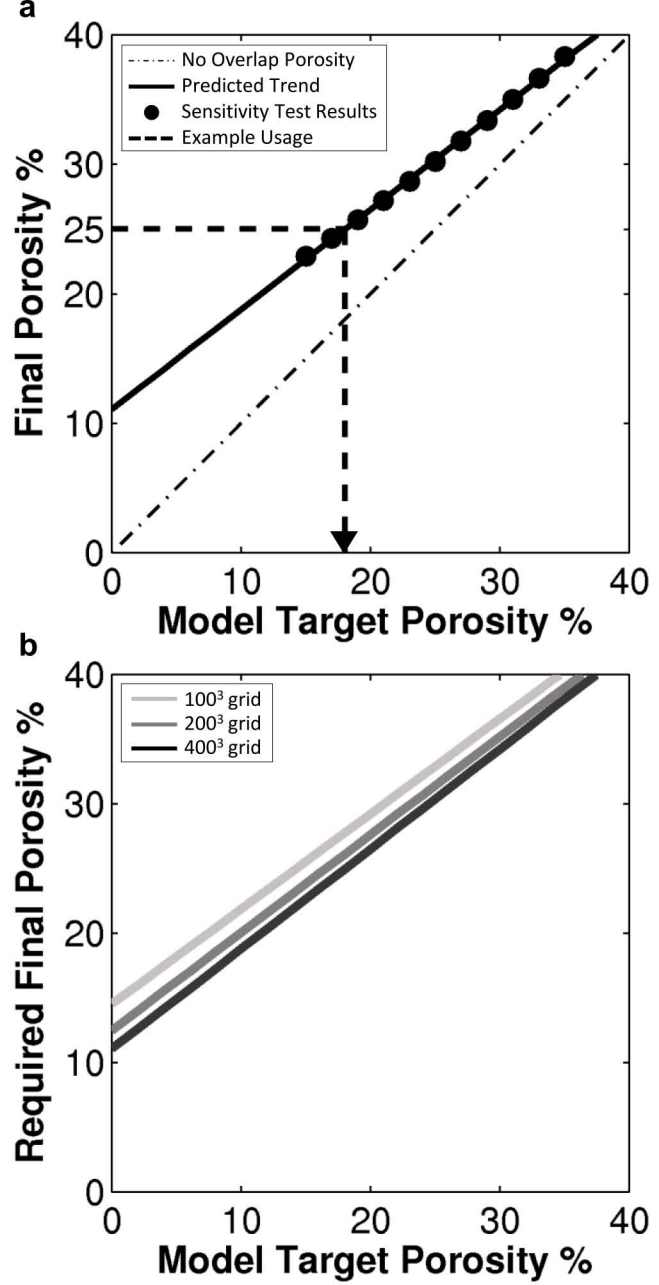
a
No Overlap Porosity
Predicted Trend
Sensitivity Test Results
Example Usage
Final Porosity %
Model Target Porosity %
0
10
20
25
30
40
b
100³ grid
200³ grid
400³ grid
Required Final Porosity %
Model Target Porosity %

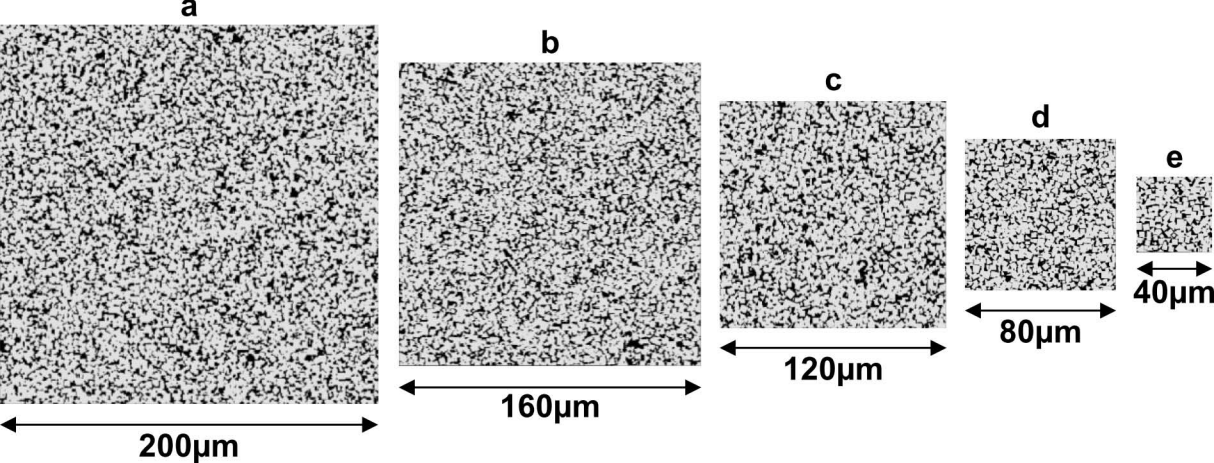
a
b
c
d
e
200μm
160μm
120μm
80μm
40μm

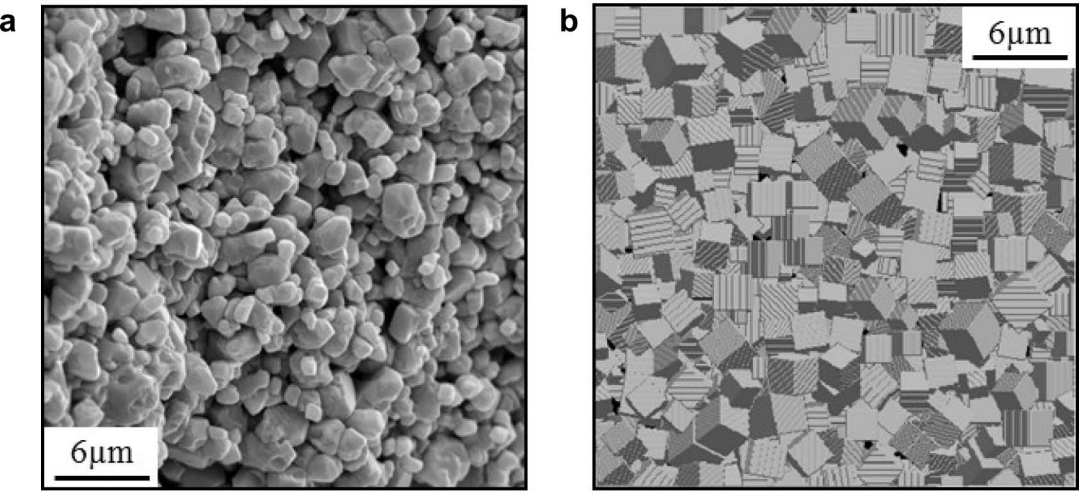
a
6μm
b
6μm

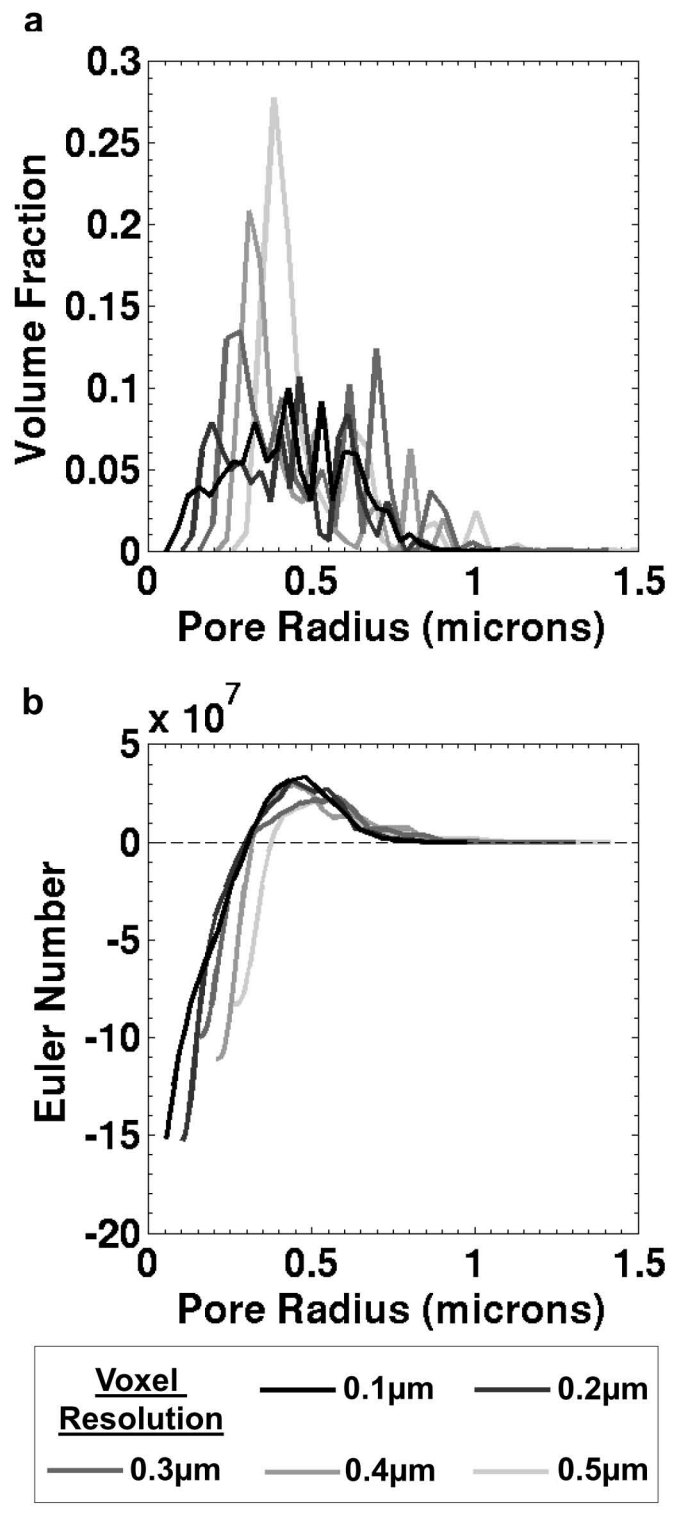
a
0.3
0.25
0.2
0.15
0.1
0.05
0
Volume Fraction
0
0.5
1
1.5
Pore Radius (microns)
b
x 10^7
5
0
-5
-10
-15
-20
Euler Number
0
0.5
1
1.5
Pore Radius (microns)
Voxel Resolution
0.1μm
0.2μm
0.3μm
0.4μm
0.5μm

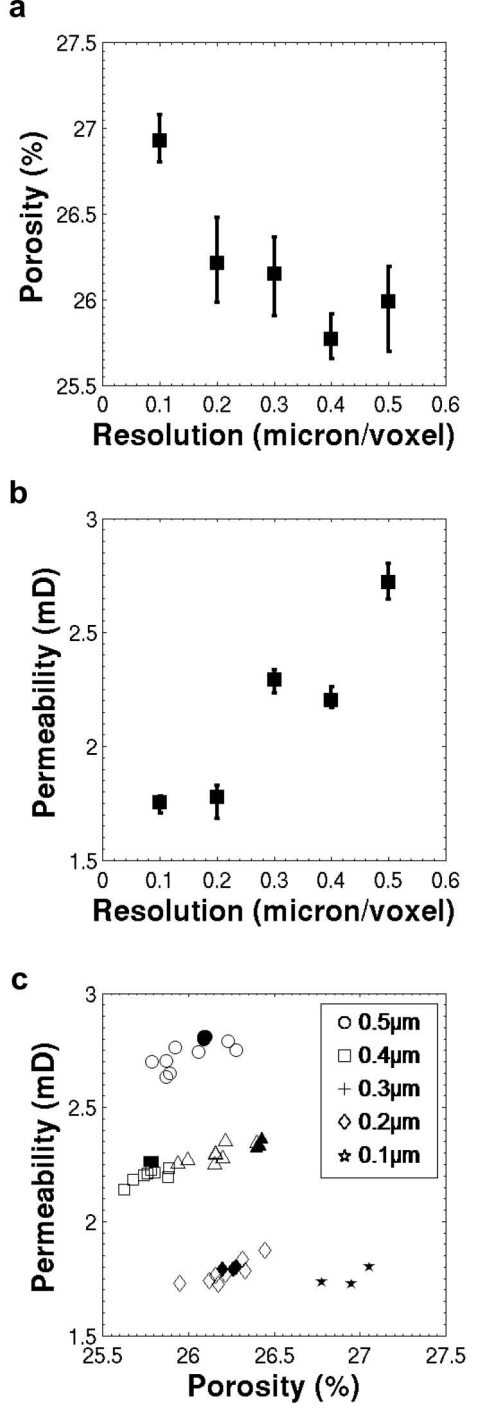
a
Porosity (%)
27.5
27
26.5
26
25.5
0
0.1
0.2
0.3
0.4
0.5
0.6
Resolution (micron/voxel)
b
Permeability (mD)
3
2.5
2
1.5
0
0.1
0.2
0.3
0.4
0.5
0.6
Resolution (micron/voxel)
c
Permeability (mD)
3
2.5
2
1.5
25.5
26
26.5
27
27.5
Porosity (%)
0.5μm
0.4μm
0.3μm
0.2μm
0.1μm

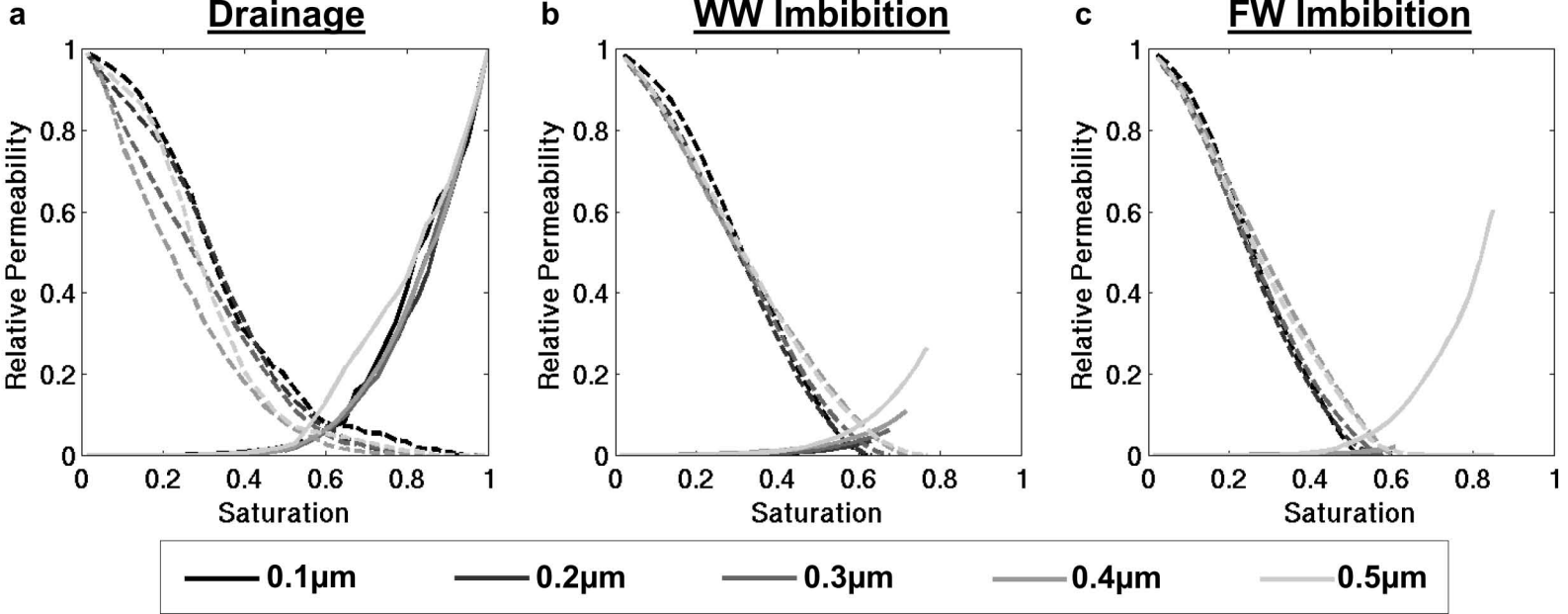
a
Drainage
b
WW Imbibition
c
FW Imbibition
Relative Permeability
Saturation
0
0.2
0.4
0.6
0.8
1
0.1μm
0.2μm
0.3μm
0.4μm
0.5μm

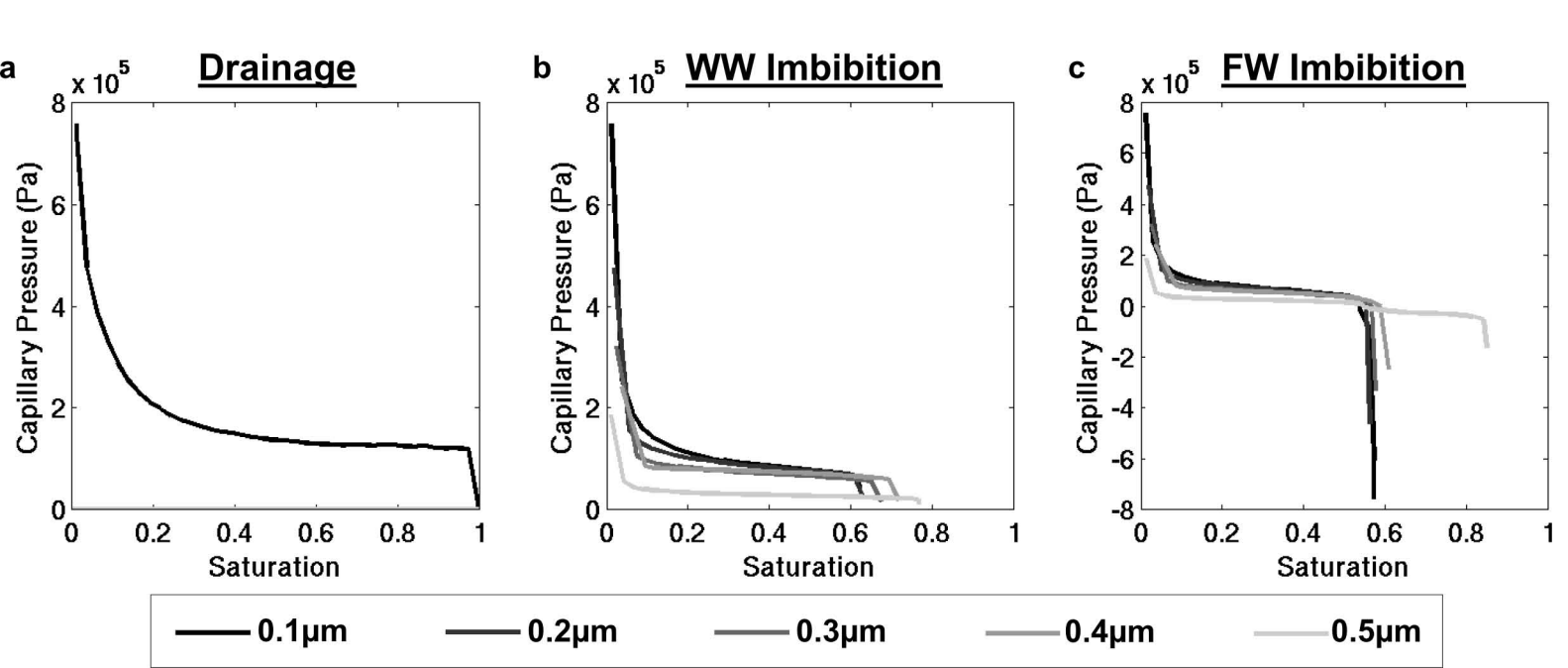
a
Drainage
x 10^5
Capillary Pressure (Pa)
Saturation
b
WW Imbibition
x 10^5
Capillary Pressure (Pa)
Saturation
c
FW Imbibition
x 10^5
Capillary Pressure (Pa)
Saturation
0.1μm
0.2μm
0.3μm
0.4μm
0.5μm

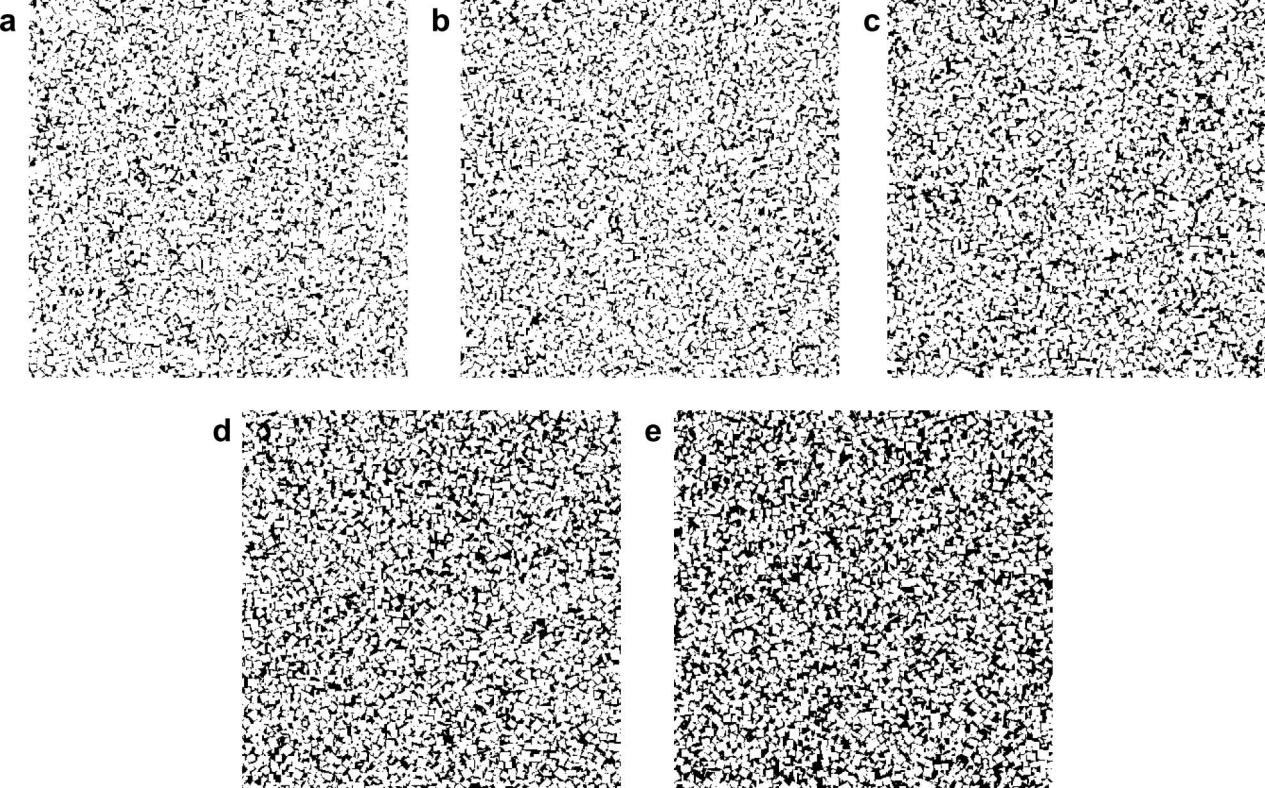
a
b
c
d
e

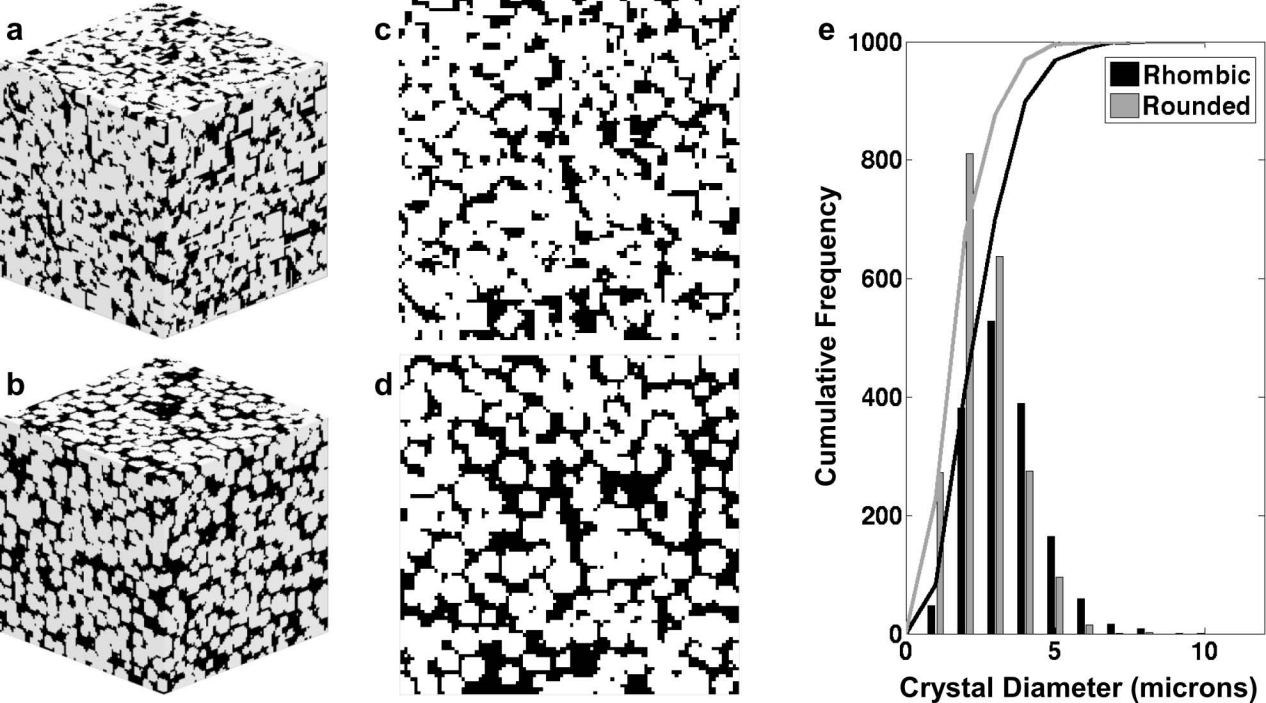
a
b
c
d
e
Rhombic
Rounded
Cumulative Frequency
Crystal Diameter (microns)
0
200
400
600
800
1000
0
5
10

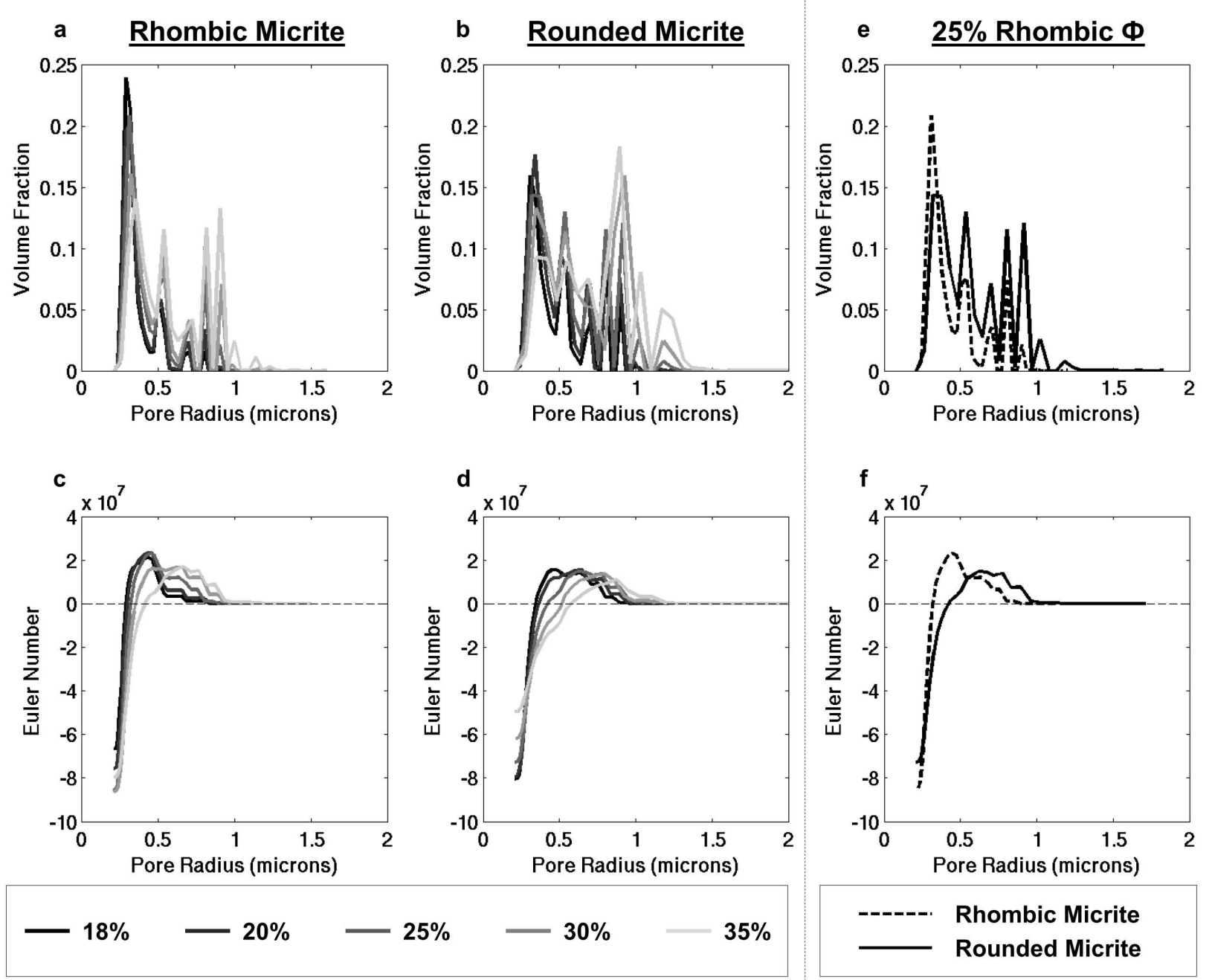
a
Rhombic Micrite
b
Rounded Micrite
e
25% Rhombic Φ
Volume Fraction
Pore Radius (microns)
c
d
f
x 10^7
Euler Number
18%
20%
25%
30%
35%
Rhombic Micrite
Rounded Micrite

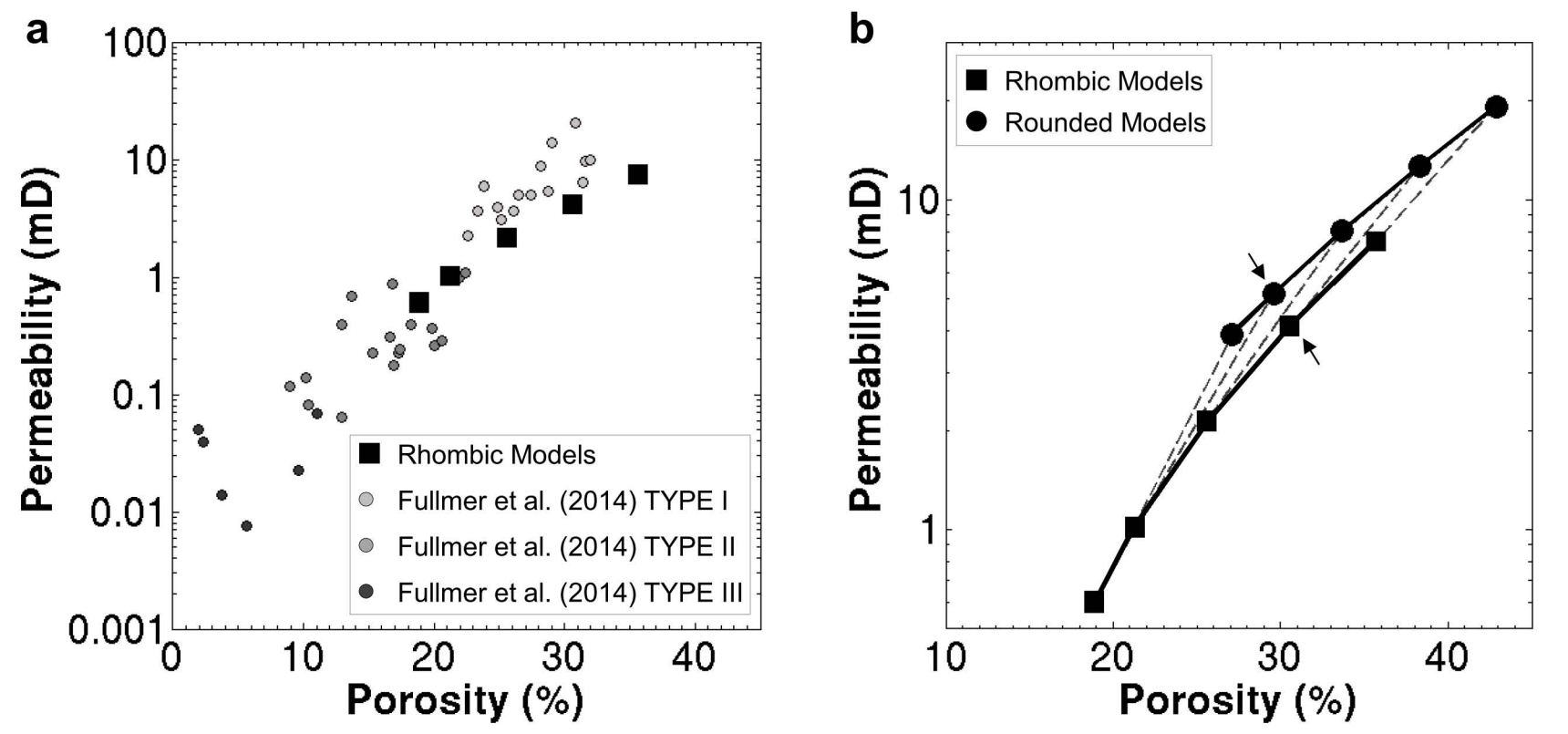
a
100
10
1
0.1
0.01
0.001
Permeability (mD)
0
10
20
30
40
Porosity (%)
Rhombic Models
Fullmer et al. (2014) TYPE I
Fullmer et al. (2014) TYPE II
Fullmer et al. (2014) TYPE III
b
Rhombic Models
Rounded Models
10
1
Permeability (mD)
10
20
30
40
Porosity (%)

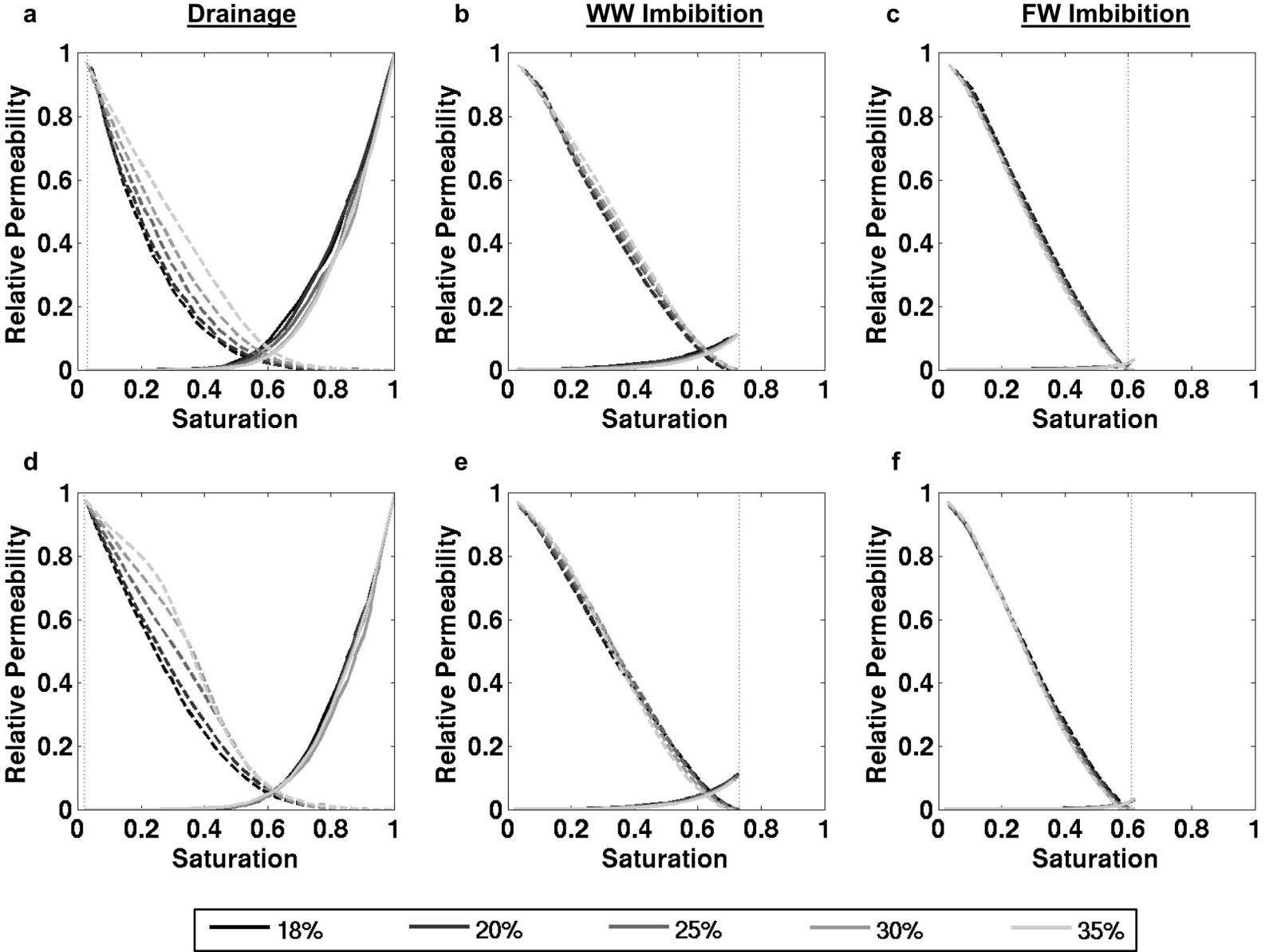
a
Drainage
b
WW Imbibition
c
FW Imbibition
d
e
f
Relative Permeability
Saturation
0
0.2
0.4
0.6
0.8
1
18%
20%
25%
30%
35%

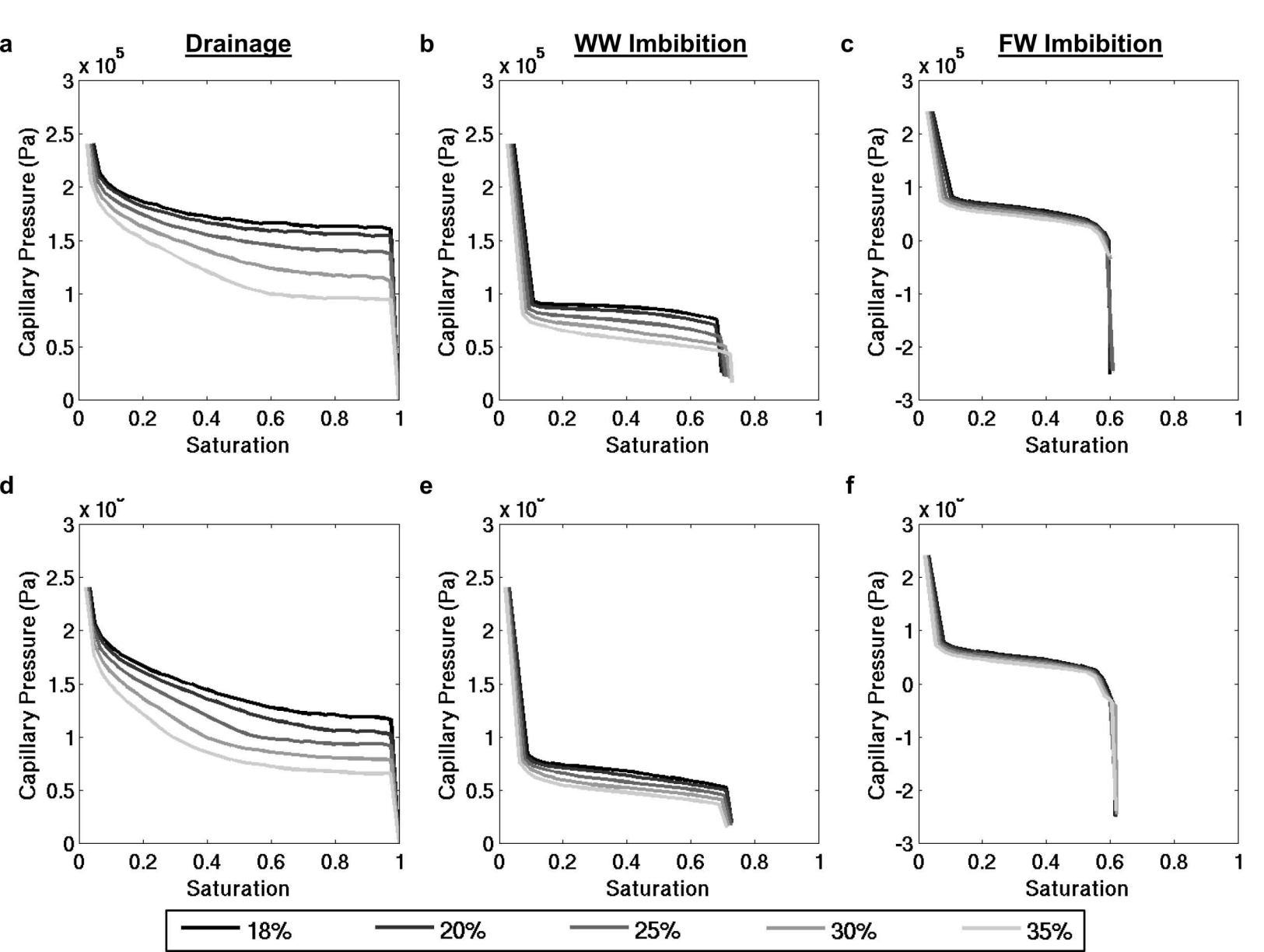
a
Drainage
b
WW Imbibition
c
FW Imbibition
d
e
f
x 10^5
x 10^
Capillary Pressure (Pa)
Saturation
18%
20%
25%
30%
35%

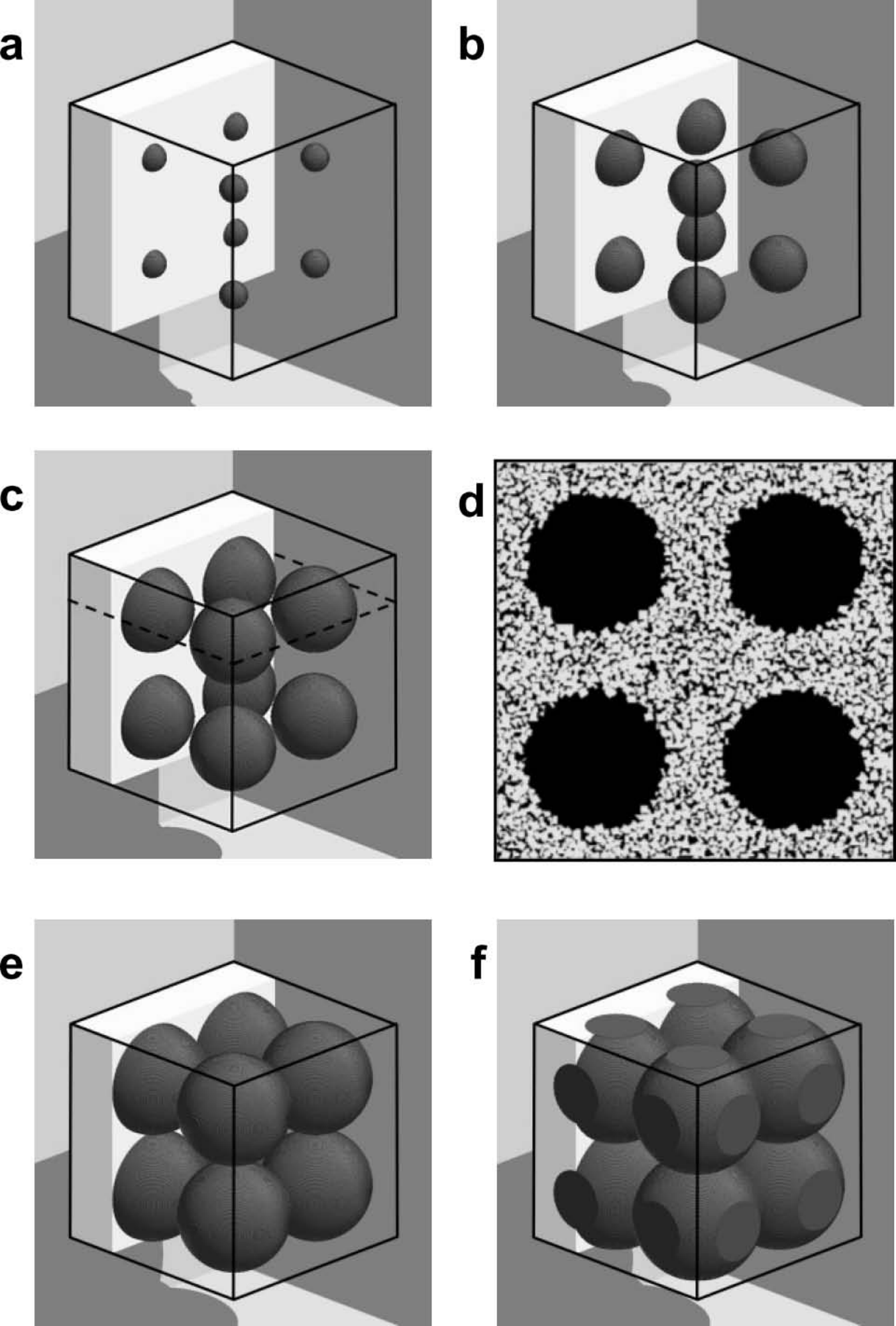
a
b
c
d
e
f

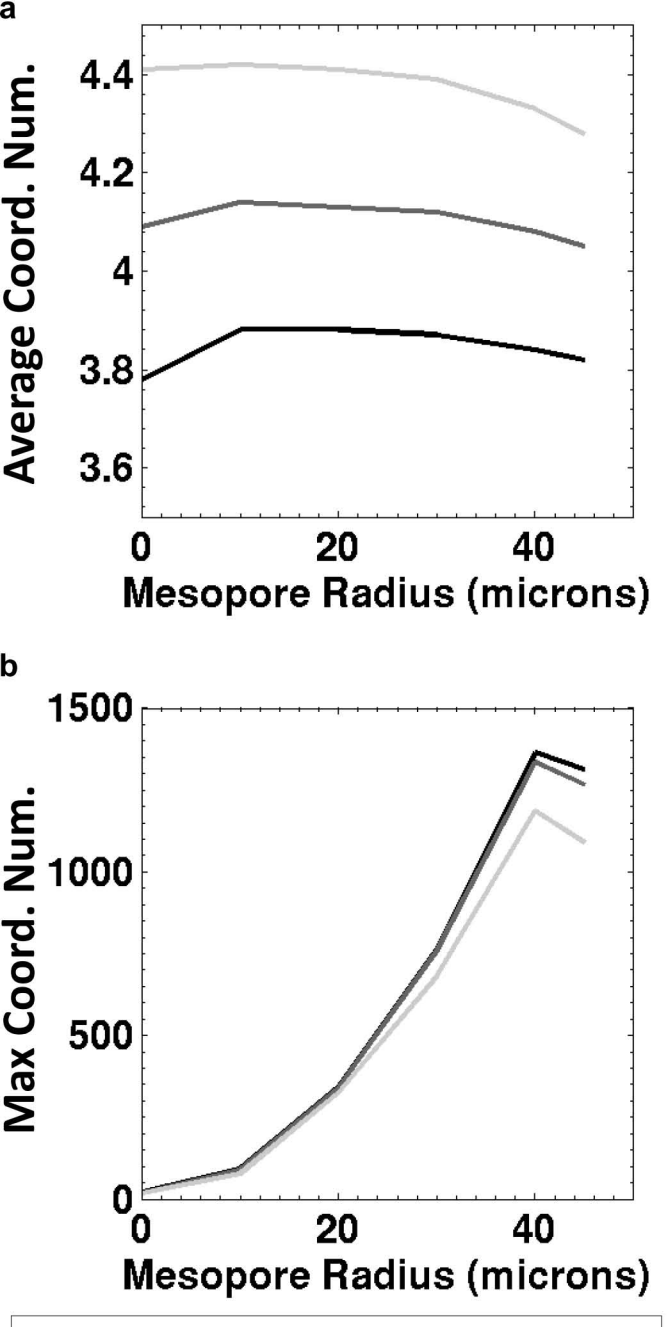
a
Average Coord. Num.
4.4
4.2
4
3.8
3.6
0
20
40
Mesopore Radius (microns)
b
Max Coord. Num.
1500
1000
500
0
0
20
40
Mesopore Radius (microns)
18% Matrix φ
25% Matrix φ
35% Matrix φ

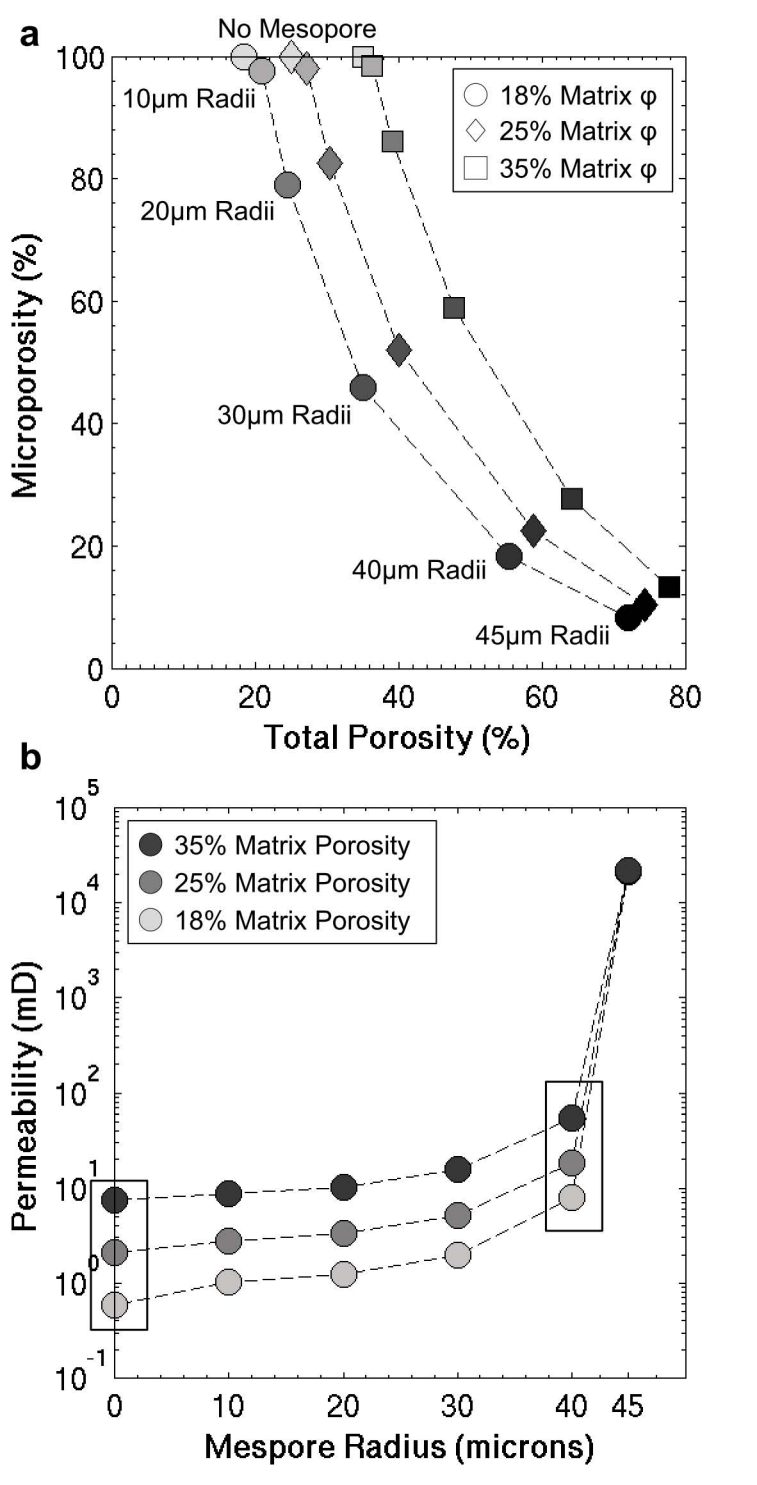
a
No Mesopore
10μm Radii
20μm Radii
30μm Radii
40μm Radii
45μm Radii
18% Matrix φ
25% Matrix φ
35% Matrix φ
Microporosity (%)
Total Porosity (%)
0
20
40
60
80
100
b
35% Matrix Porosity
25% Matrix Porosity
18% Matrix Porosity
Permeability (mD)
Mespore Radius (microns)
0
10
20
30
40
45

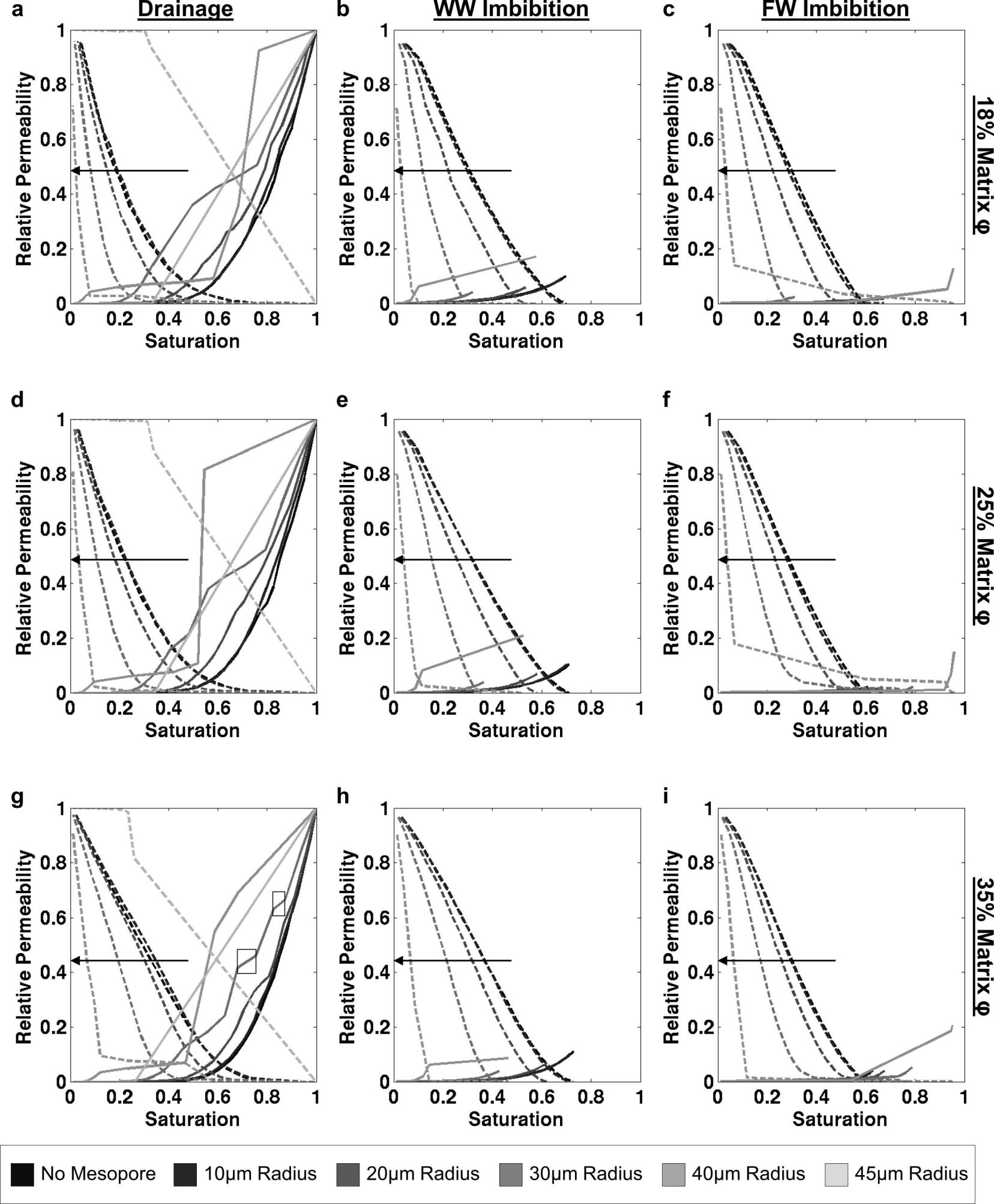
a
Drainage
b
WW Imbibition
c
FW Imbibition
18% Matrix φ
d
e
f
25% Matrix φ
g
h
i
35% Matrix φ
Relative Permeability
Saturation
0
0.2
0.4
0.6
0.8
1
No Mesopore
10μm Radius
20μm Radius
30μm Radius
40μm Radius
45μm Radius

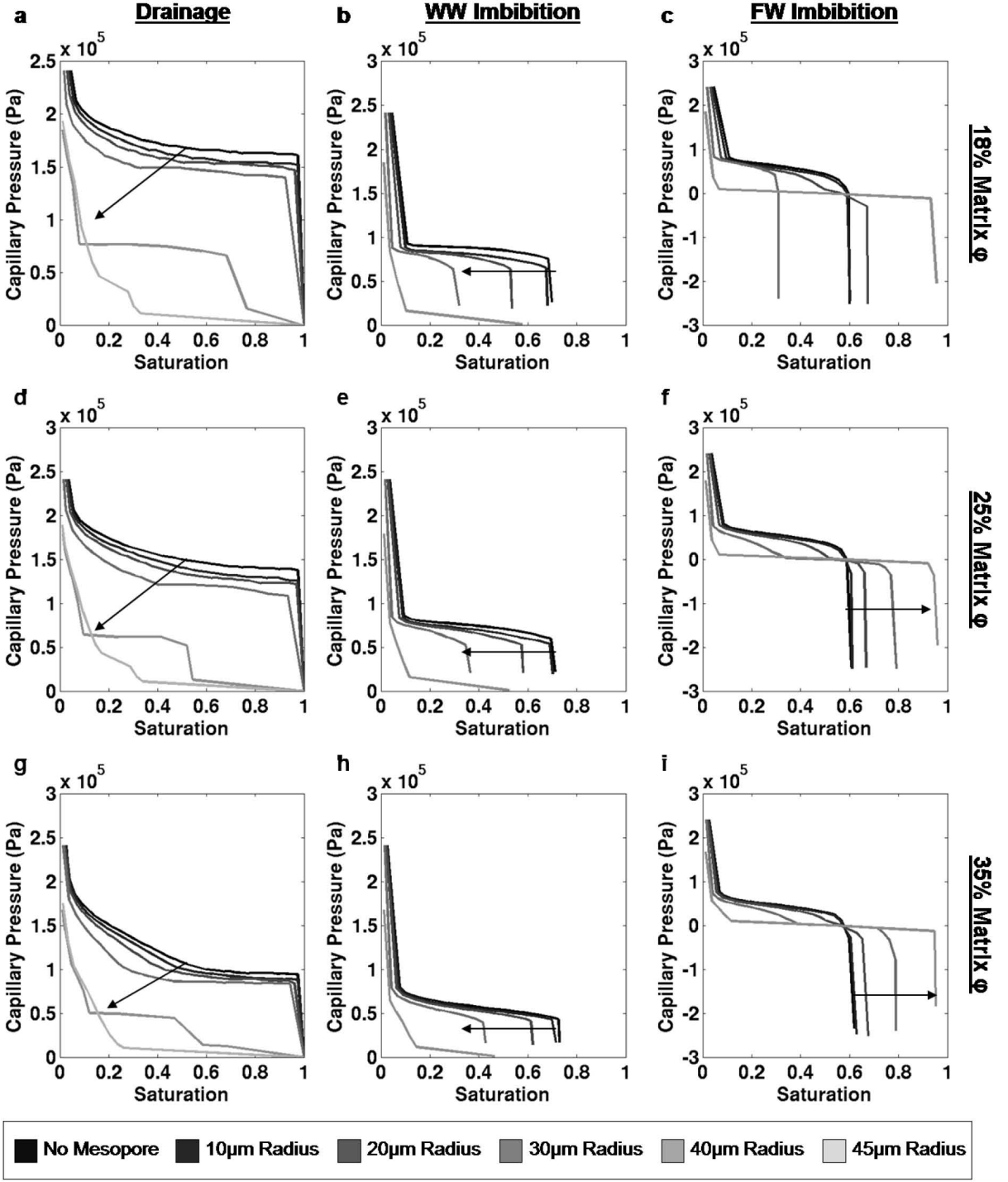
a
Drainage
b
WW Imbibition
c
FW Imbibition
18% Matrix φ
d
e
f
25% Matrix φ
g
h
i
35% Matrix φ
x 10^5
Capillary Pressure (Pa)
Saturation
No Mesopore
10μm Radius
20μm Radius
30μm Radius
40μm Radius
45μm Radius

a

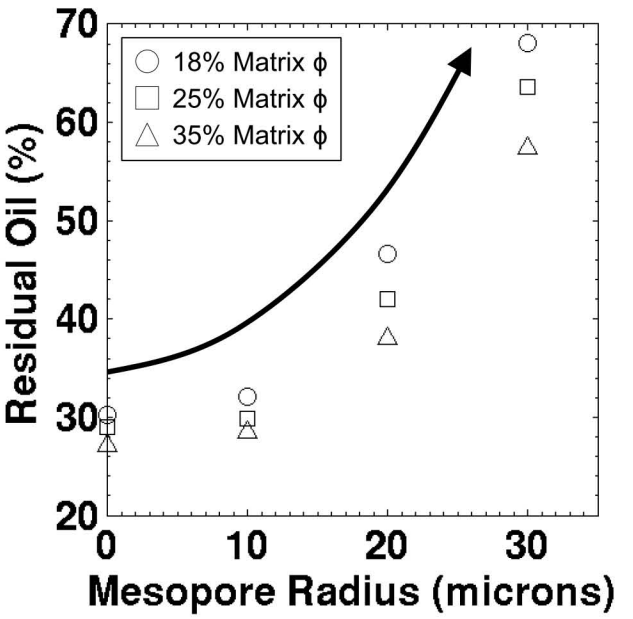
WW Imbibition
18% Matrix ϕ
25% Matrix ϕ
35% Matrix ϕ
Residual Oil (%)
70
60
50
40
30
20
0
10
20
30
Mesopore Radius (microns)

b

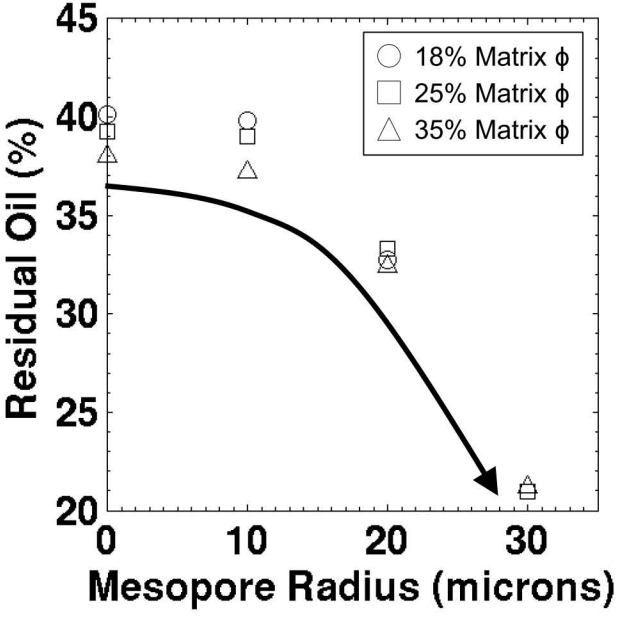
FW Imbibition
18% Matrix ϕ
25% Matrix ϕ
35% Matrix ϕ
Residual Oil (%)
45
40
35
30
25
20
0
10
20
30
Mesopore Radius (microns)